

ABSTRACT

AL ASAFEN, HADEL YOUSEF. Dorsal/NF- κ B exhibits a Dorsal-to-Ventral Mobility Gradient in the *Drosophila* Embryo. (Under the direction of Dr. Gregory T. Reeves).

Morphogen-mediated patterning is a highly dynamic developmental process. To obtain an accurate understanding of morphogen gradients, biophysical parameters such as protein diffusivities must be quantified *in vivo*. The dorsal-ventral (DV) patterning of early *Drosophila* embryos by the NF- κ B homolog Dorsal (Dl) is an excellent system for understanding morphogen gradient formation. Dl gradient formation is controlled by the inhibitor Cactus/I κ B (Cact), which regulates the nuclear import and diffusion of Dl protein. However, quantitative measurements of spatiotemporal Dl movement are currently lacking. Here, we use scanning fluorescence correlation spectroscopy to quantify the mobility of Dl. We find that the diffusivity of Dl varies along the DV axis, with lowest diffusivities on the ventral side, and the DV asymmetry in diffusivity is exclusive to the nuclei. Moreover, we also observe that nuclear export rates are lower in the ventral and lateral regions of the embryo. Both cross correlation spectroscopy measurements and a computational model of Dl/DNA binding suggest that DNA binding of Dl, which is more prevalent on the ventral side of the embryo, is correlated to a lower diffusivity and nuclear export rate. We propose that the variation in Dl/DNA binding along the DV axis is dependent on Cact binding Dl, which prevents Dl from binding DNA in dorsal and lateral regions of the embryo. Thus, our results highlight the complexity of morphogen gradient dynamics and the need for quantitative measurements of biophysical interactions in such systems.

© Copyright 2018 by Hadel Yousef Al Asafen

All Rights Reserved

Dorsal/NF- κ B exhibits a Dorsal-to-Ventral Mobility Gradient in the Drosophila Embryo

by
Hadel Yousef Al Asafen

A thesis submitted to the Graduate Faculty of
North Carolina State University
in partial fulfillment of the
requirements for the degree of
Master of Science

Chemical Engineering

Raleigh, North Carolina
2018

APPROVED BY:

Dr. Gregory T. Reeves
Committee Chair

Dr. Balaji Rao

Dr. Ross Sozzani

DEDICATION

To Mesoun and Yousef.

BIOGRAPHY

The author was raised in Abu Dhabi, United Arab Emirates. After preparation in various private schools, she joined the Petroleum Institute in Abu Dhabi and graduated with honors with BSc degree in Chemical Engineering. She got a full ride scholarship from ADNOC to do her bachelors. In August 2016, she went to the United States for graduate school. She joined the Chemical and Biomolecular department in North Carolina State University and received the 2016-2017 Provost's fellowship.

ACKNOWLEDGMENTS

To my mentor, Dr. Gregory Reeves, I couldn't have done this without you. Thank you for all of your support along the way. To my committee members, Dr. Sozzani and Dr. Rao and for all my professors who taught me a lot and influenced me to strive for excellence.

TABLE OF CONTENTS

LIST OF FIGURES	vi
Chapter 1: Introduction	1
What is developmental Biology and Why is it Important?	1
<i>Drosophila melanogaster</i> as a Genetic Model.....	1
Tissue Patterning.....	2
Dorsal Patterns the Dorsal-Ventral Axis of the <i>Drosophila</i> Embryo	2
Fluctuation Correlation Spectroscopy.....	5
Raster Image Correlation Spectroscopy (RICS).....	7
Chapter 2: Dorsal/NF-κB exhibits a Dorsal-to-Ventral Mobility Gradient in the <i>Drosophila</i> Embryo	9
Introduction.....	9
Results.....	11
Quantification of DI Diffusivity reveals a Dorsal-to-Ventral (DV) Gradient.....	11
DI Exhibits DV Variation in Nuclear Export Rate Constant	14
Dorsal Movement is Anti-Correlated with DNA Binding.....	17
Modeling Predicts DI/DNA Binding Lowers the Average Diffusivity of DI	19
Discussion	22
Materials and Methods.....	27
Fly Stocks and Preparation	27
Mounting and Imaging of <i>Drosophila</i> Embryos.....	28
RICS Analysis Using MATLAB Implementation.....	29
Pair Correlation Function (pCF) analysis using SimFCS Software.....	30
Fluorescence Recovery After Photobleaching (FRAP) Analysis	31
Mathematical Models of Nuclear Dorsal and DNA Binding.....	31
Quantification and Statistical Analysis.....	32

Data and Software Availability..... 33

LIST OF FIGURES

Figure 1.1	Dorsal patterns the dorsal-ventral (DV) axis.....	4
Figure 1.2	The Dorsal-Venus nuclear gradient is highly dynamic	5
Figure 1.3	Basics of Florescent Correlation Spectroscopy.....	6
Figure 1.4	Basics of RICS	8
Figure 2.1	RICS analysis reveals a dorsal-ventral asymmetry in the mobility of D1	14
Figure 2.2	pCF analysis and FRAP reveal a dorsal-to-ventral asymmetry in nuclear export of D1.....	17
Figure 2.3	Cross-correlation RICS analysis of DNA-bound D1.	19
Figure 2.4	One- and two-component diffusion models quantify the relationship between DNA binding and mobility of D1.	22
Figure 2.5	Variation of D1 mobility along the DV axis	22

Chapter 1 Introduction

What is Developmental Biology and Why is it Important?

Developmental Biology is the life science sector that aims in understanding can a single give rise to a completely new individual with all the incredible anatomical features that we find in multi-cellular organisms. This single cell undergoes many rounds of cell divisions to form an increasingly complex embryo which will then go on to develop various tissues and organs. It is very important in the life sciences, a key discipline in the research areas of human disease, cancer, gene therapies, and fertility. It plays an essential role in food sustainability and biological responses to environmental pollution and global warming. To study developmental biology, researchers use model systems; a simpler animal that is easier to work with and at the same time conserves all the fundamental signaling pathways. In my research I used *Drosophila melanogaster* as my genetic model.

Drosophila melanogaster as a Genetic Model

Drosophila melanogaster, known as the fruit fly or the vinegar fly. It is the uninvited guest that comes on fruit bowls every summer. It is a versatile model organism that has been used productively as a model organism for over a century to study a diverse range of biological processes including genetics and inheritance, embryonic development, learning, behavior, and aging. There are many technical advantages of using *Drosophila* over vertebrate models; they are easy and inexpensive to culture in laboratory conditions, have a much shorter life cycle, they produce large numbers of externally laid embryos and they can be genetically modified in numerous ways. Although humans and fruit flies may not look very similar, it has become well established that most of the fundamental biological mechanisms and pathways that control development and survival are conserved across evolution between these species [1]. It is the

insect behind 6 Nobel prizes in Physiology and Medicine to date with the recent one being in 2017. This tiny fly was able to contribute to medicine because of the genes humans share with *Drosophila*. An astonishing 75% of human disease genes have equivalence in flies. In particular, the genes that tell the cells how to divide, develop, and function and what the basic body plan should look like are often the same between humans and flies. This understanding yielded a wealth of discoveries. For instance, the Hedgehog (Hh) gene that is important in wing formation in *Drosophila* has a direct relative gene in humans called the Sonic Hedgehog. Studying the wing development in flies helps explain what we see when people have extra fingers or toes, which is a condition known as Polydactyly [2]. Many human diseases have been modeled in *Drosophila* such as Huntington's, addiction, and neurological diseases, including neuromuscular disease [3].

Tissue Patterning

The morphogen concept, in which a signaling gradient regulates differential gene expression in a concentration-dependent manner, forms the basis of many models of developing tissues. Morphogens send positional information to cells, depending on their location within a tissue, to command them to develop in specific ways. The roles of these signals range from the development of the initial polarities of embryos to specification of cell identity in specific tissues, and the nervous system in both vertebrates and *Drosophila* [4].

Classically, these “morphogens” have been defined as originating from a defined source and forming a graded distribution by diffusion and degradation; however, in recent years it has become clear that morphogens can become spatially organized by a variety of mechanisms.

Dorsal Patterns the Dorsal-Ventral Axis of the *Drosophila* Embryo

The NF- κ B module, conserved from flies to humans, is responsible for gene expression controlling several responses, including tissue patterning, inflammation, innate immunity, and

apoptosis. The maternal transcription factor Dorsal, homologous to mammalian NF- κ B, patterns the DV axis of the developing *Drosophila melanogaster* embryo to specify mesoderm, neurogenic ectoderm, and dorsal ectoderm cell fates [5], [6]. The I κ B homolog Cactus binds to Dorsal, retaining it outside the nuclei [7]. Toll signaling, the *Drosophila* homolog of the Interleukin 1 receptor, phosphorylates the Dorsal/Cactus complex on the ventral side of the embryo and causes Cactus to be degraded. This allows Dorsal to enter the nuclei, where it regulates gene expression [8]–[10]. Because Toll signaling is spatially asymmetric, this regulation results in a nuclear gradient of Dorsal that peaks at the ventral midline and decays to approximately 40% of the embryo's circumference (See Figure 1A). This is also illustrated in Figure 1C where the black line is an average of the Dorsal gradient in many different embryos. As shown in Figure 1B, different genes are turned on at different concentrations of Dorsal, which can be both an activator and a repressor of transcription. At high concentrations of Dorsal at the ventral side of the embryo, Type I genes such as *twist* and *snail* are expressed. In the lateral part of the embryo, intermediate Dorsal levels activate the expression of Type II genes such as *rhomboid* (*rho*), *brinker* (*brk*), *intermediate neuroblasts defective* (*ind*), and *short gastrulation* (*sog*). Dorsal acts as a repressor to Type III genes like *zerknüllt* (*zen*) and *decapentaplegic* (*dpp*), restricting their expression to dorsal regions where Dorsal concentration is the lowest [11], [12].

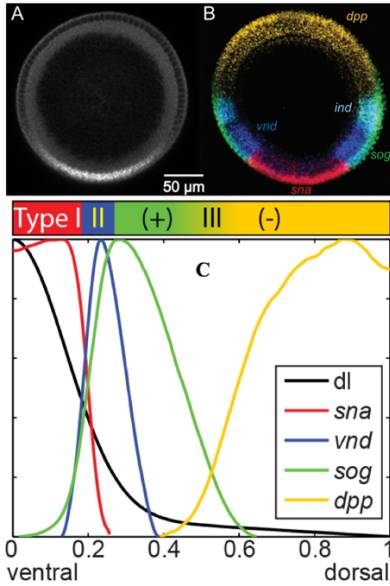


Figure.1-1: Dorsal patterns the dorsal-ventral (DV) axis. (A) Antibody staining in a fixed Dorsal-Venus embryo cross-section that is in nc 14. (B) Cross-section of late nc 14 embryo hybridized with *sna* (red), *vnd* (blue), *ind* (cyan), *sog* (green), and *dpp* (yellow) antisense RNA probes. (C) Plot of domains of gene expression for Dorsal target genes. Data comes from averages of >10 embryos for each gene. The solid black curve is average Dorsal gradient. Adapted from [11].

Dorsal nuclear gradient is dynamic, varying in time both within nuclear cycles and from nuclear cycle to the next. It oscillates in a “saw-tooth” pattern, it builds up in the ventral nuclei during interphase then disappears during mitosis, when the nuclei divide, forcing Dorsal and other nuclear factors into the cytoplasm. Later, Dorsal builds up again in the nuclei during the following interphase, as illustrated in Figure 1.2 [12]–[14]. Thus, we need an accurate and predictive mathematical model to address an outstanding question regarding the Dorsal gradient: How does a highly dynamic morphogen signal specify gene expression domains.

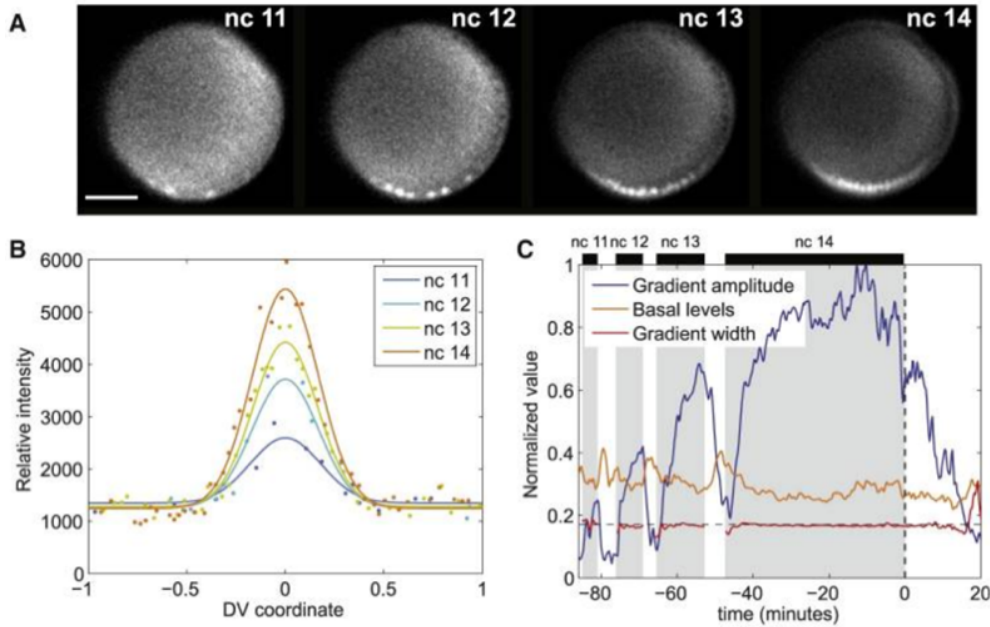


Figure.1-2: The Dorsal-Venus nuclear gradient is highly dynamic. (A) Snapshots of the Dorsal-Venus nuclear gradient for nuclear cycles 11–14. (B) Quantification of the Dorsal-Venus nuclear gradient from snapshots shown in (A). (C) Gradient amplitude (blue), basal levels (orange), and gradient width (red) from nuclear cycles 11–14.

Adapted from [11].

Fluctuation Correlation Spectroscopy

To unravel important biological questions, it is important to understand better molecular concentration, dynamics and organization at high temporal and spatial resolution. Single-point fluorescence correlation spectroscopy (FCS) is an approach used to study molecular dynamics in the microsecond-to-millisecond time range in cells and tissues. Originally developed by Magde et. al [15] for solutions then by Berland et. al [16] for cells. In this tool, light from an optical microscopy, such as Confocal microscopy, is focused on a small number of fluorescent molecules in a small illumination volume (Figure 1.3 A) defined by a confocal volume. More importantly, the selectivity of fluorescence allows only the molecule of interest to be detected. The fluorescence intensity is fluctuating due to Brownian motion of the molecules which means that

the number of fluorescent molecules in the excitation volume is randomly changing around the average number. Fluorescence fluctuations are analyzed using the autocorrelation function $G(\tau)$ to get the diffusion coefficients (Figure 1.3 C). This approach provides high temporal resolution information about protein concentrations and dynamics in a very small volume of the cell. However, there are some limitations of this technique, such as lack of spatial information, and the FCS measurements and imaging cannot be done simultaneously [17]–[19].

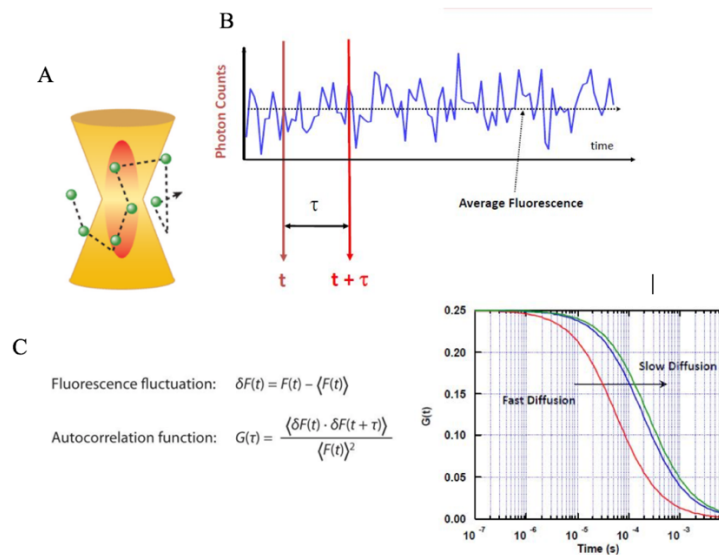


Figure 1-3: Basics of Fluorescent Correlation Spectroscopy. (A) Fluorescent molecules diffusing through the volume of observation (red oval). (B) Fluorescence correlation spectroscopy analysis and the dashed line indicates the average fluorescence. (C) The equation for the autocorrelation function, where the brackets indicate the average over all time sequences and a plot of the ACF plotted in a log scale. Adapted from [17].

Image correlation spectroscopy (ICS), developed by Petersen et. al [20], [21], is capable of getting information about concentration, degree of aggregation of proteins, average number of aggregates in the cell membrane, temporal correlations between images collected in time series [22], and spatial correlations due to flow [23]. However, ICS was based on the assumption that nothing moves on time scale of the frame acquisition. So, it has been mostly used to study fixed or slow moving molecules. To be able to get the previously inaccessible temporal windows,

raster image correlation spectroscopy (RICS) was developed. RICS allows to bridge the timescales of FCS and ICS and provide spatially resolved information in the microseconds to seconds time range [24].

Raster Image Correlation Spectroscopy (RICS)

The RICS approach is based on the principle of taking a raster scan, which implies taking multiple line scans, during the formation of the confocal image. It can exploit the time structure present in images obtained with a laser confocal microscope to spatially correlate adjacent pixels that are a fraction of micron and a few microseconds apart along a line a few milliseconds apart in successive lines. By exploiting this time structure, we measure dynamic processes such as molecular diffusion in the microsecond to second timescale [24]. It rapidly measures during the scan many focal points within the cell providing the same concentration and dynamic information of FCS as well as information on the spatial correlation between points along the scanning path. Longer time dynamics are recovered from the information in successive lines and frames. While taking the images, the Point Spread Function (PSF) must overlap, and as a fluorescent molecule moves it will be observed in neighboring pixels as the raster scans across. In the case of a slower particle, it is more likely to be observed in immediately adjacent pixels for a short period of time, resulting in a spatial correlation that is well resolved in adjacent pixels but decays as it is no longer observed. Whereas, a faster particle will be observed further in space, but is less probable to be observed in adjacent pixels resulting in a characteristic spatial correlation that decays rapidly and broadens. Through the application of the Autocorrelation Function approach, diffusion coefficients are obtained through the fitting of data, as illustrated in Figure 1.4 [18], [25]–[27][18], [25]–[27].

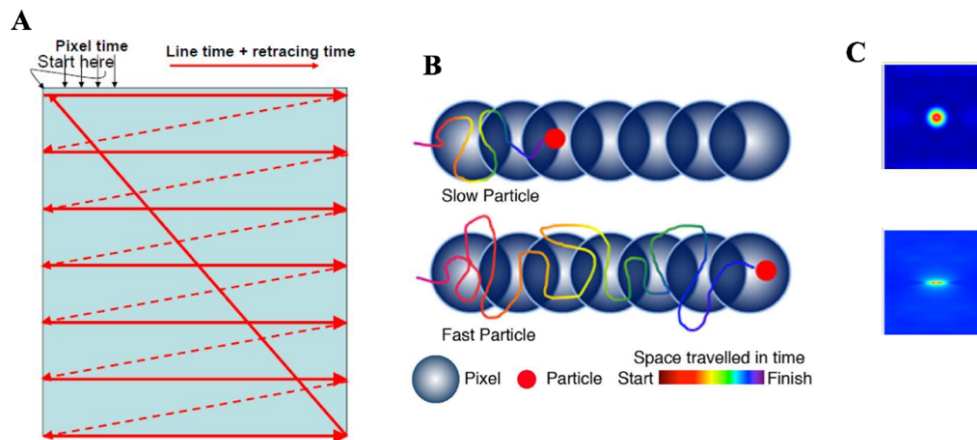


Figure 1-4: Basics of RICS. (A) The RICS approach requires an image collected with a raster scan. The laser scans across one line of the confocal image and then it resets back to the original x- position and it scans again. This implies having a fast scanning time which is in the x-direction and slow scanning time while retracing. (B) The RICS approach works on the principle that a slower moving particle will be observed across fewer pixels compared to a faster particle resulting in a spatial correlation that decays earlier. (C) The ACF for the slow-moving particle which will kind of look like a circle because it depends on the size of PSF. The ACFs for the fast diffusers will look elongated. (Adapted from [26])

Chapter 2 Dorsal/NF- κ B exhibits a dorsal-to-ventral mobility gradient in the *Drosophila* embryo

Hadel Al Asafen*, Natalie M. Clark*, Thomas Jacobsen, Rosangela Sozzani, and Gregory T. Reeves

*These authors contributed equally to this work. HA did the experiments, NMC used the SimFCS software to analyze the images, TJ did the FRAP experiment, and GTR did the image analysis. HA, NMC, and GTR wrote the manuscript.

Introduction

Tissues in a developing organism are patterned by short and long-range signaling achieved through morphogen concentration gradients, which carry the positional information necessary to control gene expression in a spatially-dependent fashion. In the past two decades, studies using GFP-tagged morphogens -- including early *Drosophila* morphogens Bicoid and Dorsal; Dpp in the wing imaginal disc; and the Hedgehog, Wnt, and TGF- β families in vertebrates -- have revealed that the establishment of morphogen gradients is a highly dynamic and complex process [11], [13], [36], [37], [28]–[35]. Live imaging studies have challenged the established view that tissue patterning relies on a constant, steady-state level of signaling to regulate gene expression [4], [38], [47], [39]–[46]. To move toward a quantitative understanding of morphogen signaling, several key biophysical parameters related to gradient formation, including movement through tissues and the effect of receptor binding on nuclear import/export rates, must be measured.

Dorsal (Dl), one of three homologs to mammalian NF- κ B [48], acts as a morphogen to pattern the dorsal-ventral (DV) axis. Dl is initially distributed uniformly along the DV axis [6], [49]. After the 9th nuclear division cycle, when the nuclei migrate to the periphery of the

syncytial embryo, Dl begins to accumulate in ventral nuclei, and is excluded from dorsal nuclei [6], [49]. This DV gradient in Dl nuclear concentration is due to signaling through the Toll receptor on the ventral side of the embryo [50]–[52]. In the absence of Toll signaling, Dl remains bound by the cytoplasmic tethering protein Cactus, the *Drosophila* IκB homolog [53], [54], and thus localized to the cytoplasm [8], [55]–[57]. On the ventral side, Toll signaling acts through Pelle kinase to phosphorylate Cactus (Cact), which causes dissociation of the Dl/Cact complex and degradation of Cact [58]. Once freed from binding to Cact, Dl enters the nucleus and regulates the expression of more than 50 target genes, which initiate further signaling pathways and specification of the embryo’s germ layers [9], [59]–[62]. Toll signaling also phosphorylates Dl, which has been shown to increase Dl nuclear localization [57], [63]–[65]. Thus, even in the absence of Cact, a shallow Dl nuclear concentration gradient is established [8], [66], [67].

While this well-established mechanism rapidly initiates Dl gradient formation, recent work has revealed complex dynamics in the further maturation of the gradient. In particular, live imaging of fluorescently-tagged Dl proteins has shown that the Dl nuclear gradient grows slowly during interphase and collapses during mitosis [11], [13]. Quantification of the gradient levels has shown that, over the course of nuclear cycle 10-14, Dl (both nuclear and cytoplasmic) accumulates on the ventral side of the embryo, causing the spatial peak of the Dl gradient to grow steadily over time [11], [12], [68], [69]. In particular, diffusion and nuclear capture of Dl, both of which are regulated by Cact, are proposed to control the continuous growth of the Dl gradient peak [68]. However, the diffusivity and nuclear transport rates are not quantitatively known. Therefore, to fully understand the dynamics of Dl gradient formation, measurements of the biophysical parameters of Dl mobility (specifically diffusivity and nuclear transport rates) are needed.

Here we use scanning fluorescence correlation spectroscopy (scanning FCS) methods to measure the diffusivity and nuclear transport of Df in live embryos. Scanning FCS techniques involve rapid and repeated acquisition of fluorescent imaging data using confocal microscopy. First, we use one scanning FCS method called Raster Image Correlation Spectroscopy (RICS) to autocorrelate GFP-tagged Df over space and time in a small region of the embryo [18], [24]. Statistics of this autocorrelation function are then analyzed to infer protein diffusion, which reveals that the diffusivity of Df-GFP varies along the DV axis. In addition, we use Pair Correlation Function (pCF) to calculate the correlation between two pixels along a line scan and visualize barriers to Df movement [70], [71]. By combining pCF with Fluorescence Recovery After Photobleaching (FRAP), we show that the nuclear export rate also varies along the DV axis. RICS and pCF data on mutants that mimic the Df gradient at different DV positions support these results. Cross-correlation RICS (ccRICS), which uses two different fluorophores (GFP and RFP, in this case), and modeling of DNA/Df/Cact interactions suggest that the DV variation in both diffusivity and nuclear export rate is the result of a higher fraction of Df binding to the DNA on the ventral side than on the dorsal side. Thus, by incorporating experimentally determined parameters into our mathematical model, we show that regulation of Df nuclear transport is important for maintaining the DV gradient in Df diffusivity.

Results

Quantification of Df Diffusivity Reveals a Dorsal-to-Ventral (DV) Gradient

To measure the diffusivity of Df in the embryo, we performed Raster Image Correlation Spectroscopy (RICS) analysis on embryos carrying a monomeric GFP-tagged Df and an H2A-RFP construct in a Df heterozygous background (hereafter referred to as Df-GFP embryos). We performed RICS analysis ($n = 150$ total number of images) on nuclear cycle 12-14 embryos,

when the DI gradient is clearly defined and detectable. Specifically, we rapidly imaged small (pixel size $\leq 0.1 \mu\text{m}$) regions of the ventral, lateral, or dorsal portions of the embryo, which have differing levels of nuclear versus cytoplasmic DI-GFP fluorescence (Figure 2.1A, Figure S1A-D and Movies S1-3). To infer the diffusivities from these raster scans, we calculated a 3D autocorrelation function (ACF; Figure 2.1B and Equation 1 in Materials and Methods) that has a fast (ξ) and slow (η) direction due to the rapid movement and line retracing of the confocal scan, respectively (Fig. 1B,C). We then fit a one-component diffusion model to this ACF (see Figure 2.1C and Equation 2 in Materials and Methods). We found that the DI diffusion coefficient varied with the position along the DV axis, with the diffusion coefficients being lowest on the ventral side of the embryo ($D = 1.1 \pm 0.8 \mu\text{m}^2/\text{s}$) and higher in lateral ($2.3 \pm 0.3 \mu\text{m}^2/\text{s}$) and dorsal ($2.2 \pm 0.7 \mu\text{m}^2/\text{s}$) regions (Figure 2.1D). To test whether this trend is statistically significant, we used linear regression, and found the slope of the diffusion coefficient from ventral-to-dorsal (Figure 2.1D) to be significantly different from zero (p-value 2×10^{-7} , r^2 value 0.33). Given that on the ventral side of the embryo DI is predominantly nuclear, while on the dorsal side DI is predominantly cytoplasmic, it is possible that the spatial variation in the diffusivity arises from differences in the behavior of nuclear and cytoplasmic DI. Therefore, we calculated the autocorrelation function (ACF) for the nuclei and the cytoplasm separately. We found a ventral-to-dorsal trend (p-value 4×10^{-8} , r^2 value 0.39; Figure 1E) in the diffusivity of nuclear-localized DI-GFP (ventral: $0.7 \pm 0.8 \mu\text{m}^2/\text{s}$; lateral: $1.7 \pm 0.4 \mu\text{m}^2/\text{s}$; dorsal: $2.6 \pm 1.6 \mu\text{m}^2/\text{s}$). However, the cytoplasmic diffusivities (ventral: $2.0 \pm 0.7 \mu\text{m}^2/\text{s}$; lateral: $2.7 \pm 0.5 \mu\text{m}^2/\text{s}$; dorsal: $2.2 \pm 0.6 \mu\text{m}^2/\text{s}$) showed no statistically significant trend in spatial variation (p-value 0.13, r^2 value 0.034; Figure 2.1F). These results suggest that the observed gradient in DI movement is specific to nuclear-localized DI.

We reasoned that the gradient in movement of nuclear-localized DI could be dependent on Toll signaling, which phosphorylates DI and increases its affinity for the nucleus [57], [63]–[65]. To this end, we performed RICS analysis on three mutant lines with “ventral-like” (*Toll^{10B}*; Schneider et al., 1991), “lateral-like” (*Toll^{r4}*; Schneider et al., 1991), or “dorsal-like” (*pll^{2/7}*; Anderson and Nüsslein-Volhard, 1984) levels of nuclear DI-GFP (Fig. S1E-G). If the spatial gradient in DI movement depends on Toll signaling, then we would expect *Toll^{10B}* embryos to have the lowest diffusivity, while *Toll^{r4}* and *pll^{2/7}* embryos would have higher diffusivity. Accordingly, we found the diffusivity of total (nuclear + cytoplasmic) DI-GFP is correlated to the extent of DI nuclear localization across the mutants (*Toll^{10B}*: $1.5 \pm 0.8 \mu\text{m}^2/\text{s}$; *Toll^{r4}*: $2.4 \pm 0.6 \mu\text{m}^2/\text{s}$; *pll^{2/7}*: $2.7 \pm 0.6 \mu\text{m}^2/\text{s}$; Fig 1D, right side). Additionally, linear regression revealed a ventral-to-dorsal trend (p-value 2×10^{-8} , r^2 value 0.35; Figure 2.1C). Similarly, the diffusivity of nuclear DI-GFP varies across the mutants (*Toll^{10B}*: $0.9 \pm 0.7 \mu\text{m}^2/\text{s}$; *Toll^{r4}*: $1.4 \pm 1.1 \mu\text{m}^2/\text{s}$; *pll^{2/7}*: $3.1 \pm 1.6 \mu\text{m}^2/\text{s}$; Figure 2.1E) with a statistically significant trend (p-value 2×10^{-6} , r^2 value 0.32). While we did see a variation in cytoplasmic DI-GFP diffusivity in the mutants (*Toll^{10B}*: $2.1 \pm 0.8 \mu\text{m}^2/\text{s}$; *Toll^{r4}*: $2.6 \pm 0.6 \mu\text{m}^2/\text{s}$; *pll^{2/7}*: $2.6 \pm 0.7 \mu\text{m}^2/\text{s}$; Figure 2.1F), the trend was weak (p-value 0.01, r^2 value 0.08), suggesting that the difference in total DI-GFP is predominantly due to changes in nuclear diffusivity of DI-GFP. Taken together, our RICS data on both wildtype and mutant embryos show that the diffusivity of nuclear DI is highly correlated to the spatial gradient in Toll signaling, while the diffusivity of cytoplasmic DI is largely unaffected by Toll signaling.

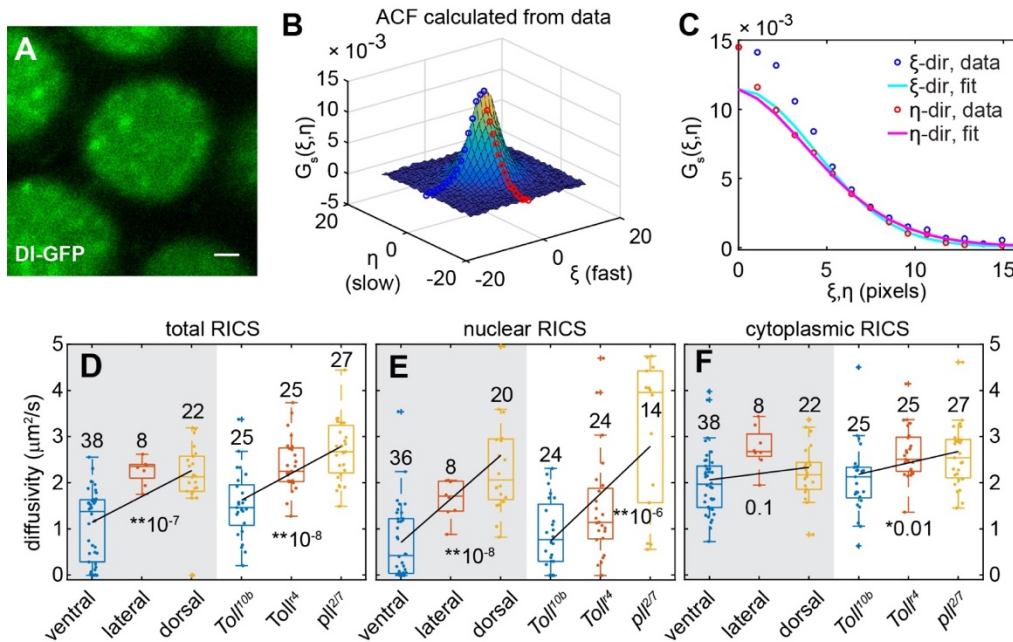


Figure 2-1: RICS analysis reveals a dorsal-ventral asymmetry in the mobility of DI. (A) Representative image of DI-GFP used for RICS analysis. Scale bar = 1 μm. (B,C) Plots of the autocorrelation function (ACF) of the image in A. (B) 3D plot of the ACF. Blue and red open circles represent the slice of the 3D surface for the fast and slow directions, respectively. (C) Plot of the fast and slow slices of the 3D ACF. Blue and red open circles (experimental data) correspond to those found in (B). The experimental data (open circles) are fit using a diffusion model (solid curves). The data and fit are separated into two components, the “fast” (ξ, blue/cyan) and “slow” (η, red/magenta) directions. (D-F) Boxplots of the diffusivity of DI-GFP measured using RICS on the entire imaging frame (nuclear plus cytoplasmic) (D), nuclear regions only (E), or cytoplasmic regions only (F). The left side of the plots (gray) contains wildtype embryos, while the right side (white) contains mutant embryos. Blue represents ventral/“ventral-like”, orange represents lateral/“lateral-like”, and yellow represents dorsal/“dorsal-like” measurements. Solid dots represent individual measurements. Black line is a linear regression fitted to the data. p-values for the slope of the trendline being zero are indicated on the graph. Sample sizes indicated on graph.

DI Exhibits DV Variation in Nuclear Export Rate Constant

Our RICS analysis revealed that DI movement is lowest on the ventral side, where it is primarily nuclear localized, and highest on the dorsal side, where it is primarily cytoplasmic.

Thus, we reasoned that nuclear import and export rates of DI could also vary spatially. First, to

determine whether there is spatial variation in DI movement into or out of the nucleus, we used Pair Correlation Function (pCF) analysis to measure any restriction of movement of DI-GFP across the nuclear envelope. In contrast to RICS, which uses raster scans of the embryo, pCF requires a line scan across the nucleus (Figure 2.2A, top row). Pixels outside and inside of the nucleus are then correlated one pair at a time to calculate the pCF carpet (Figure 2.2A, bottom row), which is then used to determine if DI-GFP can cross the nuclear envelope. We specifically calculated the Movement Index (MI) for each embryo, which represents the degree of DI-GFP movement across the nuclear envelope. A high movement index suggests that DI-GFP can cross the nuclear envelope, which is represented by an arch in the pCF carpet (demarcated by orange, dashed lines in Figure 2.2A). In contrast, a low movement index suggests that DI-GFP movement into or out of the nucleus is blocked, which is represented by a fully black column in the pCF carpet (demarcated by green, solid lines in Figure 2.2A). We separated our images into two groups, those with high movement ($MI > 0.5$) and those with low movement ($MI \leq 0.5$). We found that DI-GFP is able to move into the nucleus across the spatial regions of the embryo, as the ventral, lateral, and dorsal regions all have a majority of images with high MI values (ventral: 92.86%; lateral: 94.44%; dorsal: 100.00%) (Figure 2.2B). However, the ventral and lateral regions have significantly fewer images with high MI values when DI-GFP is measured leaving the nucleus (ventral: 64.29%; lateral: 72.22%; $p < 0.07$, Chi-squared test with likelihood ratio), suggesting that DI-GFP movement out of the nucleus is restricted in the ventral and lateral regions of the embryo (Figure 2.2B). In contrast, on the dorsal side of the embryo, almost all of the images measuring DI-GFP movement out of the embryo have high MI values (94.44%). To test whether this restricted movement out of the nucleus may be dependent on Toll signaling, we also performed pCF analysis in *Toll^{10B}*, *Toll^{r4}*, and *pll^{2/7}* mutant lines (Figure S2A), and similarly

found that a lower proportion of images in “ventral-like” mutants have high MI indices when Dl-GFP movement is measured out of the nucleus (*Toll*^{10B}: 96.15% in versus 72.73% out; $p < 0.05$, Chi-squared test with likelihood ratio) (Figure 2.2B). This suggests that the lower diffusivity of Dl-GFP in ventral and lateral nuclei is due to a restriction of Dl movement out of the nucleus, and this restriction of nuclear export rate correlates with the spatial gradient in Toll signaling.

While pCF analysis suggests that the Dl-GFP nuclear export rate is lower on the ventral side of the embryo, this method does not quantify the nuclear import and export rates. Thus, to provide an independent measure of the nuclear import and export rates, we also performed Fluorescence Recovery After Photobleaching (FRAP) experiments on either the ventral or dorsal sides of the embryo (Figure 2.2C; see also Figure S2B,C and Movies S4-S5). We found that the nuclear export rate, k_{out} , was significantly lower on the ventral side ($0.14 \pm 0.09 \text{ min}^{-1}$) than on the dorsal side ($0.56 \pm 0.29 \text{ min}^{-1}$; p -value 0.007; Figure 2.2D). However, the nuclear import rate was not significantly different on the two sides of the embryo (ventral: $0.31 \pm 0.2 \text{ min}^{-1}$; dorsal: $0.40 \pm 0.3 \text{ min}^{-1}$; p -value 0.3; Figure 2.2D). Thus, our pCF results, combined with our FRAP measurements, suggest there is a mechanism that maintains Dl nuclear localization on the ventral side of the embryo.

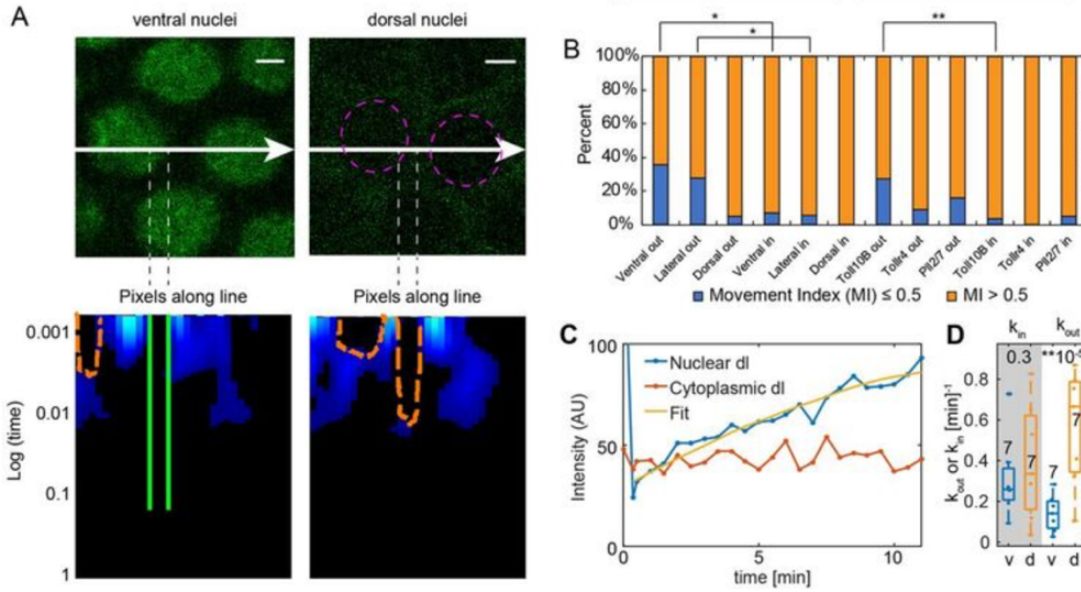


Figure 2-2: pCF analysis and FRAP reveal a dorsal-to-ventral asymmetry in nuclear export of DI. (A)

Representative images of DI-GFP on the ventral (top left image) and dorsal (top right image) sides of the embryo with their respective pCF carpets (bottom left and bottom right). Scale bar = 2µm. Arrow represents the direction of the line scan. Magenta circles in dorsal side image outline the two nuclei crossed by the line scan. White, dashed line represents areas where DI-GFP movement is measured out of the nucleus. Orange, dashed lines in the carpet label arches which indicate delayed DI-GFP movement, while green, solid lines demarcate black regions of the carpet which indicate no DI-GFP movement. **Figure 2-3(continued):** (B) Percent of embryos that have high (Movement Index (MI) > 0.5, orange) and low (MI ≤ 0.5, blue) DI-GFP movement either out of (out) or into (in) the nucleus. * denotes p<0.07, ** denotes p<0.05, Chi-squared test with likelihood ratio. (C) Representative trace of nuclear (blue) and cytoplasmic (red) DI-GFP fluorescence in the FRAP experiments. Yellow curve is the fit of the fluorescence recovery equation. (D) Boxplots of the nuclear import (left side, gray background) or export (right side, white background) rate constants measured using FRAP on either the ventral (v) or dorsal (d) regions of the embryo. p-values testing if the rate constants on the ventral side are equal those on the dorsal side are indicated on the graph. Sample sizes indicated on graph.

Dorsal movement is anti-correlated with DNA binding

One possible explanation for our findings that both the nuclear diffusivity and nuclear export rate of DI-GFP varies with position along the DV axis is that there is a substantial pool of

DI-GFP bound to DNA on the ventral side of the embryo. To determine whether such a pool exists, we used cross-correlation RICS (ccRICS; [52]) to measure the extent to which DI (DI-GFP) and Histone (H2A-RFP) may be bound to the same physical structure (in this case, DNA). We found that the ratio of the cross-correlation function (CCF) amplitude to the ACF amplitude (Fig. 3A,B), which is a relative measure of the degree to which DI-GFP and H2A-RFP are correlated, varies along the DV axis (Figure 2.3C; Digman et al., 2009). In some cases with high amplitude ratios, the overlap between DI-GFP and H2A-RFP can be seen visually (Figure S3A and Movie S6). In wildtype embryos, the ratio of amplitudes is significantly higher on the ventral side (0.24 ± 0.21) than in the lateral (0.11 ± 0.14) or dorsal (0.05 ± 0.14) regions of the embryo (p-value 3×10^{-4} , r^2 value 0.18 Figure 2.3C). Furthermore, in both the lateral and dorsal regions, the correlation between histone and DI is indistinguishable from zero. In these cases, the low correlation can be seen as the lack of peak in the CCF (compare Figure S3B to S3C). In mutant embryos, the ratio of amplitudes is also correlated with the levels of Toll signaling (*Toll^{l0B}*: 0.4 ± 0.3 ; *Toll^{r4}*: 0.1 ± 0.2 ; *pll^{2/7}*: -0.05 ± 0.4 ; Figure 2.3C) with a statistically significant trend (p-value 4×10^{-7} , r^2 value 0.29). Furthermore, the ratio of amplitudes is indistinguishable from zero in *pll^{2/7}* mutants. The ratio of amplitudes is also negatively correlated with diffusivity, which implies that, when DI-GFP is more strongly associated with the same physical structure as H2A-RFP (high CCF to ACF ratio), the diffusivity of DI-GFP is lower (p-value 3×10^{-7} , r^2 value 0.16; Figure 2.3D). Overall, the finding that the cross correlation between DI-GFP and H2A-RFP is negatively correlated to diffusivity suggests that DNA binding of DI may be responsible for its lowered diffusivity and lowered nuclear export rate on the ventral side of the embryo.

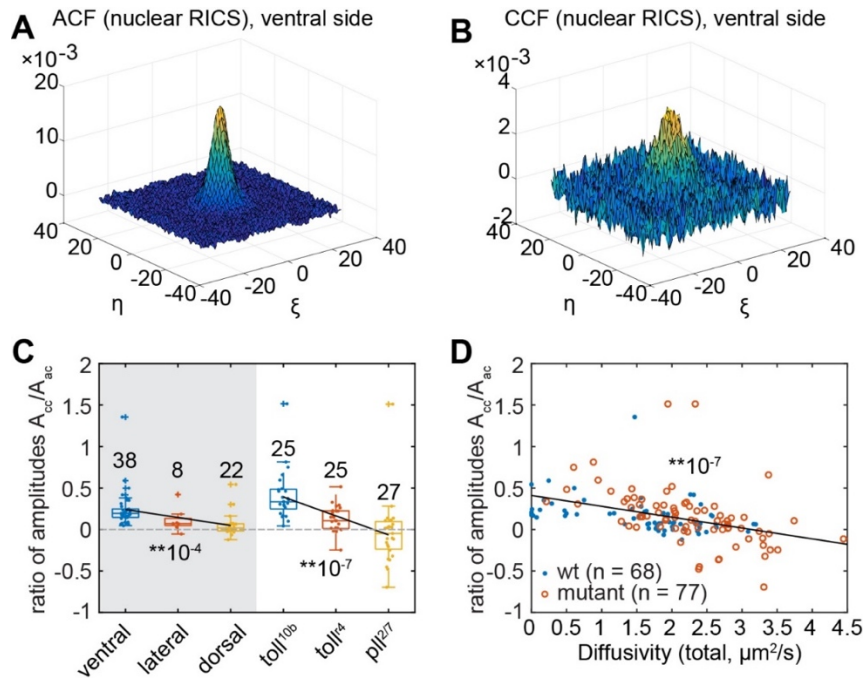


Figure 2-4(continued): Cross-correlation RICS analysis of DNA-bound DI. (A) Autocorrelation function of DI-GFP, with nuclear mask, on ventral side. (B) Cross-correlation between DI-GFP and H2A-RFP, with nuclear mask, from same image used to calculate (A). (C) Boxplot of the ratio of the cross-correlation amplitude to the autocorrelation amplitude (A_{cc}/A_{ac}). The left side of the plots (gray) contains wildtype embryos, while the right side (white) contains mutant embryos. Blue represents ventral/”ventral-like”, orange represents lateral/”lateral-like”, and yellow represents dorsal/”dorsal-like” measurements. Solid dots represent individual measurements. Black line is a linear regression fitted to the data. p-values for the slope of the trendline being zero are indicated on the graph. Sample sizes indicated on graph. (D) Plot of the ratio A_{cc}/A_{ac} (y-axis) versus diffusion coefficient returned by RICS (x-axis). Blue solid dots represent measurements from wild type embryos, while red open circles are measurements from mutant embryos. Black line is a linear regression fitted to the data. p-value for the slope of the trendline being zero are indicated on the graph. Sample sizes indicated in legend.

Modeling predicts DI/DNA binding lowers the average diffusivity of DI

Our cross-correlation results suggest that the spatial variation in DI movement could be due to a population of DI that is bound to DNA. Given our RICS and pCF results that DI movement is slower on the ventral side of the embryo, we further reasoned that the DNA-bound DI has a slower diffusion coefficient than the cytoplasmic DI. Thus, to test if the spatial variation

in D1 movement is due to DNA binding, we compared two diffusion models. The first is a one-component model that has only one parameter that can be varied to fit the model to the data, which is the diffusivity of D1 (Equation 2). This one-component model assumes all D1 is freely diffusible, and that none is bound to DNA. Further, the one-component model was used to fit the ACFs from RICS and infer the diffusion coefficients of D1-GFP shown in Fig. 1. The second model is a two-component diffusion model (Equations S32-S35) in which nuclear D1 could be in two states: freely diffusible and DNA-bound (Figure 2.4A; see Supplemental Methods for more information). The two-component model contains two additional parameters that are allowed to vary: the rate constants of DNA binding (k_{on}) and dissociation (k_{off}). We first tested if fitting a one-component model to a two-component system accurately recapitulates the experimentally determined average diffusion coefficient, as the previous RICS analysis assumed a one-component model (Figure 2.1D-F). We found that fitting the one-component model to a simulated two-component autocorrelation function (ACF) yields an average diffusivity between zero and $2.3 \mu\text{m}^2/\text{s}$, which is similar to the range of our experimentally determined values from RICS. Further, we found the average diffusivity to be strongly correlated with the simulated fraction of D1 bound to DNA in the two-component model, which is $1-\phi$ (Figure 2.4 B,C and Fig. S4A-F; see Materials and Methods section for definition of ϕ). When a large fraction of D1 is diffusible ($\phi = 0.9$; Figure 2.4B), the one component model fits the data well and predicts a reasonable diffusivity ($D = 1.4 \mu\text{m}^2/\text{s}$; Figure 2.4B). On the other hand, when D1 is largely bound to DNA ($\phi = 0.3$; Figure 2.4C), the one component model predicts a very low diffusivity ($D = 0.028 \mu\text{m}^2/\text{s}$; Figure 2.4C). This low diffusivity correlates with the two slices of the ACF (the fast and slow direction) collapsing onto each other (Figure 2.4C and Figure S4 A,B,F). This suggests that the lower diffusion values observed on the ventral side of the embryo could be due

to a large proportion of DNA-bound DI. In support of this, when we fit the two-component model to our experimental ACFs, the two-component model fits the ACFs better than the one-component model (Figure 2.4D). Taken together, these results suggest that our experimental data are indicative of a two-component system where a proportion of DI is bound to DNA.

Finally, we used our one- and two-component models to determine if the low average diffusivity measured in the one-component model correlates with a high proportion of DNA-bound DI in the two-component model. Accordingly, we found that, when the one component model predicts a low diffusivity, the two component model predicts a high fraction of DNA-bound DI (p-value 9×10^{-9} , r^2 value 0.48; Figure 2.4E). These results are also observed in a three component model of free DI, DI/Cact complex, and an immobile DI/DNA complex (see Figure S4G-M and Supplemental Experimental Procedures), suggesting that the nuclear DI bound to Cact could mechanistically explain the DV asymmetry in the ability of DI to bind DNA. In summary, our multiple component modeling shows that DI binding to DNA only on the ventral side of the embryo could explain the DV asymmetry in DI mobility.

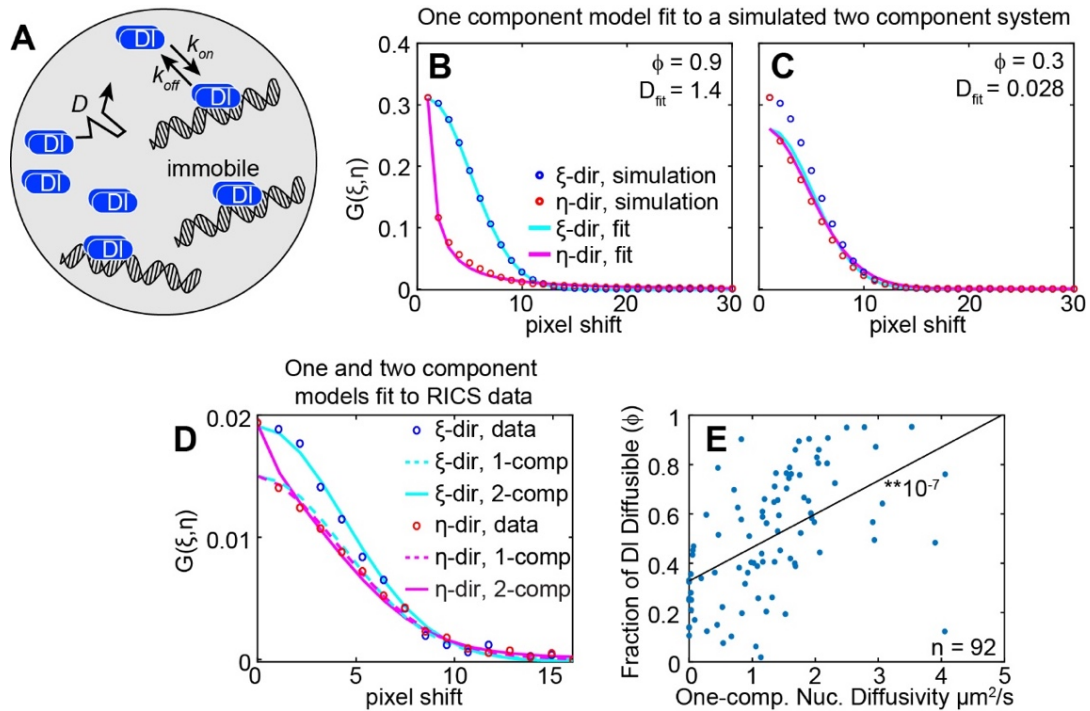


Figure 2-5: One- and two-component diffusion models quantify the relationship between DNA binding and mobility of Df. (A) Illustration of the two-component model. Df (blue circles) can diffuse and reversibly bind DNA. Df bound to DNA is immobile. In contrast to the one-component diffusion model, in which Df is freely diffusible and does not bind to DNA. (B,C) One-component diffusion model (solid curves) fit to a simulated two-component autocorrelation function (ACF) (open circles) for (B) 90% freely diffusible Df and 10% DNA-bound Df ($\phi = 0.9$) and (C) 30% freely diffusible Df and 70% DNA-bound Df ($\phi = 0.3$). The data and fit are separated into two components, the “fast” (ξ , blue/cyan) and “slow” (η , red/magenta) directions. (D) Comparison of one-component (dashed curves) and two-component (solid curves) diffusion models fit to experimental RICS data (open circles). (E) Plot of the proportion of free Df (ϕ , y-axis) versus the diffusion coefficient of free Df returned from the one-component diffusion model (x-axis). Black line is a linear regression fitted to the data. p-value for the slope of the trendline being zero is indicated on the graph. Sample size indicated on graph.

Discussion

In this study, we used fluorescence fluctuation spectroscopy methods, as well as photobleaching experiments, to quantify the movement of a GFP-tagged Df protein in the 2-3 hr old *Drosophila* embryo (Fig. 5A). Our measurements ultimately revealed a DV asymmetry in the

mobility of D1, which was correlated to a similar DV asymmetry in the ability of D1 to bind to DNA. First, RICS analysis showed that D1 diffusivity varies along the DV axis, in particular within the nucleus (Fig. 5B). Moreover, the results obtained from the pCF and FRAP experiments showed that there is also variation in the movement of D1 out of the nuclei: on the ventral side, nuclear export of D1 is not as rapid as it is on the dorsal side (Fig. 5C). Given that our measurements show variation in the mobility of D1 along the DV axis, and that the variation is associated with nuclear-localized D1, we hypothesized that D1 is binding more efficiently to the DNA on the ventral side than on the dorsal side (Fig. 5D). Variation in DNA-binding efficiency would explain both the lower diffusivity and nuclear export rate constant measurements on the ventral side of the embryo. Therefore, we used ccRICS to test this. The amplitude of the CCF, when normalized by the amplitude of the ACF, is a measure of the extent to which D1-GFP is bound to the DNA. The ratio varied significantly along the DV axis: specifically, it was large on the ventral side and low on the dorsal side. Further, this ratio correlates with the DV asymmetry of our diffusivity measurements. Thus, these results suggest restricted nuclear D1 movement on the ventral side of the embryo correlates with a high proportion of DNA-bound D1.

Given the possibility that at least two pools of D1 exist in the nucleus (free vs DNA bound), we built a two-component model that accounts for both pools of D1. Using this model, in conjunction with a one-component model in which all D1 is freely diffusible, we found that lower diffusivities in the one-component model correspond to a large fraction of D1 bound to DNA in our RICS data. In addition, we found the two-component model, compared to the one-component model, fits our data better. While the one-component model gives an estimate of average diffusivity, the two-component model estimates $K_{nuc} = k_{on}/k_{off}$, or, equivalently, the ratio of

free DI to DNA bound DI. Taken together, our results suggest that there is a DV asymmetry in the efficiency with which DI can bind to the DNA. On the ventral side of the embryo, a significant fraction of DI binds DNA, which is correlated with a low diffusivity of nuclear DI, and likely contributes to a low nuclear export rate constant. In contrast, on the dorsal side, the very small amount of nuclear DI binds the DNA at a low frequency, and also has a high diffusivity and nuclear export rate.

What could be causing the DV variation in DI mobility and DI/DNA interactions (Figure 2.5E,F)? One possibility is the Toll-mediated phosphorylation of DI on the ventral side of the embryo (Figure 2.5F). Accordingly, Toll signaling not only disrupts DI/Cact complex, but also phosphorylates DI to potentiate its entry into the nucleus [57], [63]–[65]. Thus, at least in part, Toll signaling likely explains the lower nuclear export rate constant on the ventral side. In support of this, our mutant analysis shows that the DV gradient in DI movement correlates with the Toll signaling gradient. On the other hand, if a significant fraction of DI is immobilized on the ventral side, this would entail a lower value for the measured nuclear export rate and movement index, which implies that DI/DNA interactions are also likely to play a part in the lowered nuclear export rate. And while it is possible that phosphorylated DI, in addition to its higher affinity for the nucleus, also gains a higher affinity for DNA binding (and thus has a slower mobility on the ventral side), no support for such an altered affinity for DNA has been previously shown.

Therefore, we propose that, in addition to Toll signaling possibly reducing the nuclear export rate on the ventral side, the presence of DI-GFP/Cact complex in the nuclei on the dorsal side of the embryo may reduce the DI/DNA binding (and thus, increase average DI diffusivity), as well as increase the measured nuclear export rate (Figure 2.5E). If nuclear DI on the dorsal

side is free Dl, and not Dl/Cact complex, then it should have the same ability to bind DNA as free Dl in ventral nuclei, and thus the mobility should be the same. However, if the predominant species in the dorsal-most nuclei is Dl/Cact complex, then it would have high average mobility, owing to the fact that it cannot bind DNA [53], [54]. Accordingly, our recent modeling work has shown that the presence of Dl/Cact complex in the nuclei explains the dynamics of Dl-Venus measurements, as well as downstream gene expression, while free Dl alone cannot [11], [12], [69]. In comparison, mammalian I κ B, the homolog of Cact, enters the nucleus to regulate NF- κ B dimers [74]. Furthermore, newly-formed NF- κ B/I κ B complexes are then rapidly exported from the nuclei; if a similar relationship holds in *Drosophila*, the presence of Dl/Cact complex would also explain the higher nuclear export rate on the dorsal side of the embryo.

Primarily, Cact acts to tether Dl to the cytoplasm and prevent nuclear translocation. Indeed, loss of Cact function permits intermediate levels of Dl to enter the nuclei, even on the dorsal side of the embryo. However, recent secondary, positive roles for Cact in the formation of the Dl gradient have been discovered. Because Cact is degraded on the ventral side of the embryo, there is a DV gradient of Dl/Cact complex, which results in a ventrally-directed net flux of Dl [68]. Furthermore, recent experimental work has suggested a pool of Cact fragments, which are refractory to Toll signaling, are able to bind and potentiate Dl signaling on the ventral side of the embryo, possibly through transport as well [67]. In addition to these roles for Cact in establishing the Dl gradient, our proposed mechanism of Cact-mediated regulation of Dl levels inside the nuclei further highlights the multifaceted nature of Cact function. Thus, incorporating quantitative measurements of the Dl/Cact complex should be the next step towards gaining future insights into morphogen signaling and mechanisms required for embryonic patterning.

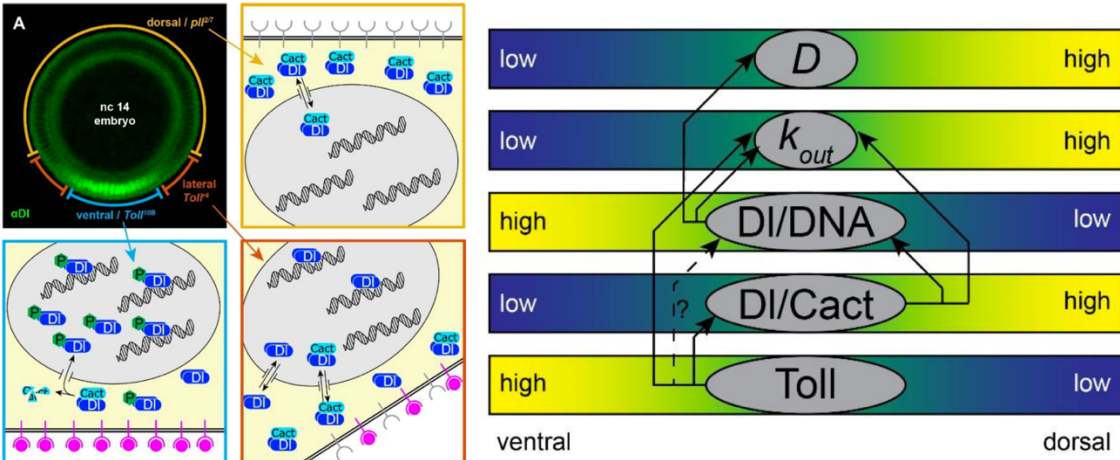


Figure 2-6: Variation of DI mobility along the DV axis. (A) (top left) Depiction of the different embryo domains, ventral (blue region), lateral (orange region), and dorsal (yellow region). (bottom left) Schematic of ventral side of embryo. High levels of activated Toll (magenta receptors) result in the destruction of Cact and phosphorylation of DI. Free DI enters the nucleus, so GFP fluorescence is mostly nuclear. Free DI in the nucleus binds to DNA, which lowers the overall mobility of DI species, and exits the nucleus at a slow rate. (bottom right) Schematic of lateral domain of embryo. Lower levels of Toll activation lead to a mixture of free and Cact-bound DI. Nuclear and cytoplasmic levels of GFP fluorescence are roughly equal. DI has a higher mobility due to lower fraction of DI bound to the DNA. DI exits the nucleus faster than on the ventral side. (top right) Schematic of the dorsal domain of the embryo. Little-to-no free DI is present, so DI-GFP fluorescence is mostly cytoplasmic. High mobilities stem from no DNA binding. (B-E) Graphical summary of the DV asymmetry in the data. (B,C) Both diffusivity (one-component RICS measurement) and nuclear export rate constant (one component bleaching recovery model) are low on the ventral side and high on the dorsal side. (D) The binding efficiency between DI and DNA is high on the ventral side and low on the dorsal side. We propose that DI/DNA binding is partially responsible for the DV asymmetry in both the diffusivity and nuclear export rate measurements. (E) We propose that the presence of DI/Cact complex in the nucleus (low on ventral side; high on dorsal side) contributes to the lack of DI/DNA binding, as well as the higher nuclear export rate on the dorsal side. (F) Toll signaling (high on ventral side; low on dorsal side) also likely plays a significant part in the DV asymmetry in the nuclear export rate and may also contribute to the DV asymmetry in DI/DNA binding, in addition to its primary function to limit DI/Cact complex on the ventral side.

Materials and Methods

Fly Stocks and Preparation

Drosophila melanogaster stocks were kept on corn meal molasses food in vials or bottles at 25°C and all crosses were performed at 25°C. *Drosophila* embryos, that were about 1-2 hrs old, were collected and mounted on slides for imaging. Briefly, flies were left to deposit eggs on fresh grape juice agar plates with yeast paste for 30-45 min. Those embryos were then aged to 30 min to reach the desired developmental stage. Those embryos are then brushed from the grape juice agar plates into a mesh basket using a paint brush and DI water. The embryos were dechorionated using bleach and then washed with DI water (Carrell & Reeves 2009).

dl-mGFP (DI-GFP) was created by BAC recombineering and *dll.2.5* flies were generated by cleaning up *dll* via two homologous recombinations with *yw* (Carrell et al. 2017). Flies carrying *dll.2.5* were crossed to flies carrying H2A-RFP on the second chromosome (BS# 23651) to generate flies that have *dll.2.5*, H2A-RFP transgene on the second chromosome. H2A-RFP, *dll.2.5*, *dl-mGFP* flies were created by homologous recombination (Carrell et al. 2017). The generation of *Toll^{r4}* and *Toll^{10B}* mutant embryos has been previously described (Stathopoulos et al. 2002). Other *Drosophila* strains were obtained from the Bloomington (BL) stock center, namely *pll²* (BL3111) and *pll⁷* (BL3112).

Mounting and Imaging of *Drosophila* Embryos

Drosophila embryos that were 1-2 hrs old were mounted laterally on a microscope slide using a mixture of heptane glue (Supatto et al. 2009) and two pieces of double-sided tape to prevent sample movement (Carrell & Reeves 2015). Embryos were imaged on a Zeiss LSM 710 confocal microscope using a 40x 1.2NA water objective. Embryos in nuclear cycle 12 to 14 were selected using the H2A-RFP marker. Embryos undergoing cell division (as visualized by the

H2A-RFP marker) were not used in for analysis as cell division alters the endogenous DI distribution.

For image acquisition consistent with RICS analysis, a 256 x 256 pixel region of interest of the embryo was selected for measurements (Supplemental Figure 1). The pixel size of the region varied from 40nm to 100nm to include different numbers of nuclei. The 488nm (green) laser intensity ranged from 0.5% to 3.0% and the 561nm (red) laser intensity ranged from 0.1% to 0.2%. The region of interest was raster scanned with a pixel dwell time of 6.30us for 200 frames (total imaging time of approximately 1.5 minutes). The range of imaging parameters is reported in Table S1.

For image acquisition consistent with pCF analysis, a 32x1 line scan through 2 to 4 nuclei was used as the region of interest (Fig. 2A). The pixel size was not set for each image but, instead, varied between 40-100nm according to the region of interest selected. The laser intensities varied as in the RICS imaging. The line was scanned with a pixel dwell time of 6.30us for 200,000 to 400,000 time points (total imaging time of approximately 1.5 to 3 minutes).

In the photobleaching experiments, embryos were dechorionated, mounted, and imaged using the same protocol as described above. Individual nuclei were chosen at random across the embryo. The following parameters were kept constant: bleaching box, ~700 pixels (26.46 microns by 26.46 microns); bleaching time (amount of time the laser bleached the nuclei), ~20 seconds; number of cycles, 30; and 488nm laser power, 50%. Each bleaching session lasted about 30 minutes (Movie S3) and was followed by imaging the entire depth of the embryo. Two nuclei per embryo were imaged in a single session.

Raster Image Correlation Spectroscopy (RICS) Analysis using MATLAB

Implementation

Analysis of time series images consistent with RICS analysis is briefly described here (see Supplementary Experimental Procedures for more information). First, for each frame i (of size 256×256 pixels) in the DI-GFP channel, a background subtraction by the average of a sliding window with a five-frame radius was performed to remove the effect of global movement of large structures [24]. Next, the average intensity of every pixel in the sliding window was added back to frame i to ensure the frame intensity was not near zero, to yield array I . Finally, to obtain the ACF for frame i , we computed the following for all pixel shifts ξ, η :

$$G_i(\xi, \eta) = \frac{\langle I(x, y)I(x + \xi, y + \eta) \rangle}{\langle I(x, y) \rangle^2}, \quad (1)$$

where the angle brackets denote ensemble average in both x and y . In practice, $G_i(\xi, \eta)$ is evaluated using the fast Fourier transform method [17]. The final ACF for total RICS, $G_s(\xi, \eta)$, was computed as the average of $G_i(\xi, \eta)$ for all frames i in the time series. Cross-correlation functions were computed in a similar way, except $I(x + \xi, y + \eta)$ was replaced by the analogous array from the H2A-RFP channel.

To compute nuclear RICS, first a nuclear mask for each frame was found. First, noise and small regions of high intensity that were not nuclei were removed from the H2A-RFP channel through morphological erosion then morphological dilation, followed by Gaussian filtering. Next, the top and bottom 2% of pixels were saturated. Hard thresholds were then applied to find objects presumed to be the nuclei. Finally, due to the previous morphological erosion operation, segmented objects were grown through morphological dilation, resulting in the nuclear mask used for nuclear RICS. The cytoplasmic mask was then found by first taking the complement of the nuclear mask, then eroding the cytoplasmic regions.

The nuclear RICS analysis proceeded the same as that for total RICS, except for each frame, the pixels outside the nuclear mask were set to zero. The resulting $G_i(\xi, \eta)$ were normalized by an array resulting from the application of Eqn (1) to the nuclear mask instead of to array I . The ACF for cytoplasmic RICS was computed analogously.

ACFs calculated from the total, nuclear, or cytoplasmic data were fit to a one component diffusion model (Fig. 1D-F; [51]):

$$G_s^{model}(\xi, \eta; A, B, D) = \frac{A \exp\left(-\frac{(r/w_0)^2}{1 + 4D \tau/w_0^2}\right)}{(1 + 4D \tau/w_0^2)\sqrt{1 + 4D \tau/w_z^2}} + B, \quad (2)$$

where $r = \Delta r \sqrt{\xi^2 + \eta^2}$, $\tau = \tau_p \xi + \tau_\ell \eta$, Δr is the pixel size in microns, τ_p and τ_ℓ are the pixel dwell time and line scan time in seconds, respectively, and w_0 and w_z are the waist sizes of the point spread function in the planar and axial directions, respectively. Equation (2) was fit to $G_s(\xi, \eta)$ using least squares and varying A, B, D . The parameters $\Delta r, \tau_p, \tau_\ell, w_0, w_z$ were microscope parameters and considered fixed. ACFs calculated from the nuclear data were fit to two-component and three-component models in the least squares sense (Fig. 4D, E). The derivation and application of these models can be found in the Supplementary Experimental Procedures.

Pair Correlation Function (pCF) Analysis using SimFCS Software

pCF analysis of the collected line scans was performed using the SimFCS software ([51]; <https://www.lfd.uci.edu/globals/>) as described in [17]. Three pixel distances of 6, 7, and 8 pixels were used as technical replicates to account for differences in sizes of nuclei. If DI-GFP showed movement out of/into a majority of nuclei (no black region or black arch in the pCF carpet), that image was assigned a movement index of 1. Otherwise, if the majority of DI-GFP showed no

movement (black vertical region in the pCF carpet), that image was assigned a movement index of 0 (Figure 2.2A). The 3 technical replicates were then averaged for each biological replicate. The analysis was repeated for the line scan in the reverse direction, resulting in 6 total technical replicates per image.

Fluorescence Recovery After Photobleaching (FRAP) Analysis

Each FRAP experiment was analyzed according to the following procedure (see Supplementary Experimental Procedures for more information). First, the image sequence was stabilized using a standard optical flow protocol, which was necessary because the embryo sometimes moved very slightly during imaging (see Supplementary Experimental Procedures; Carrell et al., 2017). Next, the H2A-RFP channel was segmented to find the nuclei and cytoplasm in a manner similar to the RICS images (see Supplementary Experimental Procedures for more information and relevant differences). The intensity of DI-GFP in the bleached nucleus was fit to a differential equation that describes nuclear import and export of DI-GFP (see Supplementary Experimental Procedures; Carrell et al., 2017), which yielded estimates of the nuclear import rate constant, k_{in} , and the import/export equilibrium constant, $K_{nuc} \equiv k_{in}/k_{out}$.

Mathematical Models of Nuclear Dorsal and DNA Binding

In the two-component model (see Figure 2.4), we assume DI is present in the nucleus in two states in equilibrium: bound to DNA and unbound. Unbound DI is free to diffuse in the nucleus with diffusivity of $2.3 \mu\text{m}^2/\text{s}$, while DNA-bound DI is immobile. DI can bind to DNA with a binding rate constant of k'_{on} and dissociates from the DNA with rate constant $k_{off} = 0.025 \text{ s}^{-1}$. We varied $K_{DNA} \equiv k'_{on}/k_{off}$, which is related to φ , the fraction of DI that is unbound, from near infinity to near zero. See Supplementary Experimental Procedures for more details.

Quantification and Statistical Analysis

Non-linear least squares was used to fit Equation (2) to the RICS ACFs. The fitted diffusivity value is t -distributed, and a standard error for the diffusivity (radius of a 68% confidence interval) was calculated. With the exception of five time course image stacks of nuclear RICS either on the dorsal side of wild type embryos, or in $pll^{2/7}$ embryos (the two cases in which nuclear intensity is very low), for all fitted diffusivities, the standard error was less than $4 \mu\text{m}^2/\text{s}$. This was used as a filter for the data; the five time course image stacks in which the standard error was greater than $4 \mu\text{m}^2/\text{s}$ were removed from analysis.

For the diffusivity of DI calculated by RICS (Figure 2.1D-F), the ccRICS data (ratio of amplitudes; Figure 2.3 C,D), and for the correlation between nuclear diffusivity and ϕ (Figure 2.4E), simple linear least squares regression was applied. The slope of the regression trend line is t -distributed with $n-2$ degrees of freedom, where n is the number of data points. Reported p -values are for t -tests with the null hypothesis that the slope is zero.

For the pCF data (Figure 2.2), a Chi-squared test with likelihood ratio was used to test if the proportion of Movement Index (MI) values that were less than 0.5 was different for movement measured into the nucleus vs movement measured out of the nucleus. The Chi-squared test was performed using JMP software (<https://www.jmp.com/>).

The FRAP data (Figure 2.2 C,D) was tested for significance by t -test. The null hypothesis was that the rate constant of nucleocytoplasmic shuttling (k_{in} or k_{out}) did not differ between ventral and dorsal sides.

For all tests, a p -value less than 0.05 was considered significant, and for the Chi-Squared test we also consider the two p -values that were less than 0.07 as significant (Figure 2.2). The statistical tests performed on each sample are listed in the Results text as well as the figure

legends. Sample sizes are indicated on the figures. Means and standard errors are reported in the Results.

Data and Software Availability

Images, tables, and sequencing results will be uploaded to a data repository, Data Dryad. Accession numbers will be available upon notification of acceptance for publication. Matlab codes will be uploaded to NCSU resource [github.ncsu.edu](https://github.com/ncsu) and will also be available from the Reeves Lab website.

REFERENCES

- [1] B. H. Jennings, “Drosophila—a versatile model in biology & medicine,” *Materials Today*, vol. 14, no. 5, pp. 190–195, 2011.
- [2] D. T. Chang *et al.*, “Products, genetic linkage and limb patterning activity of a murine hedgehog gene,” *Development*, vol. 120, no. 11, pp. 3339–3353, 1994.
- [3] T. E. Lloyd and J. P. Taylor, “Flightless flies: Drosophila models of neuromuscular disease,” *Annals of the New York Academy of Sciences*, vol. 1184, 2010.
- [4] H. L. Ashe and J. Briscoe, “The interpretation of morphogen gradients,” *Development*, vol. 133, no. 3, pp. 385–94, Feb. 2006.
- [5] K. V. Anderson and C. Nüsslein-Volhard, “Information for the dorsal-ventral pattern of the Drosophila embryo is stored as maternal mRNA,” *Nature*, vol. 311, no. 5983, pp. 223–227, 1984.
- [6] S. Roth, D. Stein, and C. Nüsslein-Volhard, “A gradient of nuclear localization of the dorsal protein determines dorsoventral pattern in the Drosophila embryo,” *Cell*, vol. 59, no. 6, pp. 1189–202, Dec. 1989.
- [7] S. Roth, Y. Hiromi, D. Godt, and C. Nüsslein-Volhard, “cactus, a maternal gene required for proper formation of the dorsoventral morphogen gradient in Drosophila embryos,” *Development*, vol. 112, no. 2, pp. 371–88, Jun. 1991.
- [8] A. Bergmann *et al.*, “A gradient of cytoplasmic Cactus degradation establishes the nuclear localization gradient of the dorsal morphogen in Drosophila,” *Mech. Dev.*, vol. 60, no. 1, pp. 109–23, Nov. 1996.
- [9] G. T. Reeves and A. Stathopoulos, “Graded dorsal and differential gene regulation in the Drosophila embryo,” *Cold Spring Harb. Perspect. Biol.*, vol. 1, no. 4, p. a000836, Oct. 2009.
- [10] J. Sen, J. S. Goltz, L. Stevens, and D. Stein, “Spatially restricted expression of pipe in the Drosophila egg chamber defines embryonic dorsal-ventral polarity,” *Cell*, vol. 95, no. 4, pp. 471–481, 1998.
- [11] G. T. Reeves, N. Trisnadi, T. V. Truong, M. Nahmad, S. Katz, and A. Stathopoulos, “Dorsal-ventral gene expression in the Drosophila embryo reflects the dynamics and precision of the dorsal nuclear gradient,” *Dev. Cell*, vol. 22, no. 3, pp. 544–57, Mar. 2012.
- [12] L. M. Liberman, G. T. Reeves, and A. Stathopoulos, “Quantitative imaging of the Dorsal nuclear gradient reveals limitations to threshold-dependent patterning in Drosophila,” *Proc. Natl. Acad. Sci. U. S. A.*, vol. 106, no. 52, pp. 22317–22, Dec. 2009.
- [13] R. DeLotto, Y. DeLotto, R. Steward, and J. Lippincott-Schwartz, “Nucleocytoplasmic shuttling mediates the dynamic maintenance of nuclear Dorsal levels during Drosophila embryogenesis,” *Development*, vol. 134, no. 23, pp. 4233–41, Dec. 2007.
- [14] J. S. Kanodia *et al.*, “Dynamics of the Dorsal morphogen gradient,” vol. 106, no. 51, pp. 21707–21712, 2009.
- [15] D. Magde, E. Elson, and W. W. Webb, “Thermodynamic fluctuations in a reacting system measurement by fluorescence correlation spectroscopy,” *Phys. Rev. Lett.*, vol. 29, no. 11, pp. 705–708, 1972.
- [16] K. M. Berland, P. T. So, and E. Gratton, “Two-photon fluorescence correlation spectroscopy: method and application to the intracellular environment,” *Biophys. J.*, vol. 68, no. 2, pp. 694–701, 1995.
- [17] M. A. Digman and E. Gratton, “Lessons in Fluctuation Correlation Spectroscopy,” *Annu.*

- Rev. Phys. Chem.*, vol. 62, no. 1, pp. 645–668, 2011.
- [18] M. A. Digman, C. M. Brown, P. Sengupta, P. W. Wiseman, A. R. Horwitz, and E. Gratton, “Measuring fast dynamics in solutions and cells with a laser scanning microscope,” *Biophys. J.*, vol. 89, no. 2, pp. 1317–1327, 2005.
- [19] N. M. Clark and R. Sozzani, “Plant Genomics,” vol. 1610, 2017.
- [20] N. O. Petersen, “Scanning fluorescence correlation spectroscopy. I. Theory and simulation of aggregation measurements,” *Biophys. J.*, vol. 49, no. 4, pp. 809–815, 1986.
- [21] N. O. Petersen, P. L. Höddelius, P. W. Wiseman, O. Seger, and K. E. Magnusson, “Quantitation of membrane receptor distributions by image correlation spectroscopy: concept and application,” *Biophys. J.*, vol. 65, no. 3, pp. 1135–1146, 1993.
- [22] P. W. Wiseman and J. A. Squierb, “Two-photon Image Correlation Spectroscopy and Image Cross- Correlation Spectroscopy,” *Microscopy*, vol. 4262, no. October, pp. 279–286, 2001.
- [23] P. W. Wiseman, “Spatial mapping of integrin interactions and dynamics during cell migration by Image Correlation Microscopy,” *J. Cell Sci.*, vol. 117, no. 23, pp. 5521–5534, 2004.
- [24] M. A. Digman, P. Sengupta, P. W. Wiseman, C. M. Brown, A. R. Horwitz, and E. Gratton, “Fluctuation correlation spectroscopy with a laser-scanning microscope: exploiting the hidden time structure.,” *Biophys J*, vol. 88, no. 5, pp. L33--L36, May 2005.
- [25] M. J. Rossow, J. M. Sasaki, M. a Digman, and E. Gratton, “Raster image correlation spectroscopy in live cells,” *Nat Protoc*, vol. 5, no. 11, pp. 1761–1774, 2010.
- [26] S. Mieruszynski, M. A. Digman, E. Gratton, and M. R. Jones, “Characterization of exogenous DNA mobility in live cells through fluctuation correlation spectroscopy,” *Sci. Rep.*, vol. 5, no. February, pp. 1–10, 2015.
- [27] D. Borja-Cacho and J. Matthews, “NIH Public Access,” *Nano*, vol. 6, no. 9, pp. 2166–2171, 2008.
- [28] T. Gregor, E. F. Wieschaus, A. P. McGregor, W. Bialek, and D. W. Tank, “Stability and nuclear dynamics of the Bicoid morphogen gradient.,” *Cell*, vol. 130, no. 1, pp. 141–52, Jul. 2007.
- [29] A. A. Teleman and S. M. Cohen, “Dpp gradient formation in the *Drosophila* wing imaginal disc.,” *Cell*, vol. 103, no. 6, pp. 971–980, Dec. 2000.
- [30] E. V Entchev, A. Schwabedissen, and M. A. González-Gaitán, “Gradient formation of the TGF β homolog Dpp.,” *Cell*, vol. 103, no. 6, pp. 981–991, Dec. 2000.
- [31] O. Wartlick *et al.*, “Dynamics of Dpp signaling and proliferation control.,” *Science (80-)*, vol. 331, no. 6021, pp. 1154–1159, Mar. 2011.
- [32] S. Zhou *et al.*, “Free Extracellular Diffusion Creates the Dpp Morphogen Gradient of the *Drosophila* Wing Disc,” *Curr. Biol.*, vol. 22, no. 8, pp. 668–675, Mar. 2012.
- [33] V. Ribes *et al.*, “Distinct Sonic Hedgehog signaling dynamics specify floor plate and ventral neuronal progenitors in the vertebrate neural tube,” *Genes Dev.*, vol. 24, no. 11, pp. 1186–1200, Jun. 2010.
- [34] P. H. Williams, A. Hagemann, M. González-Gaitán, and J. C. Smith, “Visualizing long-range movement of the morphogen Xnr2 in the *Xenopus* embryo.,” *Curr Biol*, vol. 14, no. 21, pp. 1916–1923, Nov. 2004.
- [35] T. Holzer, K. Liffers, K. Rahm, B. Trageser, S. Özbek, and D. Gradl, “Live imaging of active fluorophore labelled Wnt proteins,” *FEBS Lett.*, vol. 586, no. 11, pp. 1638–1644, Jun. 2012.

- [36] V. Wallkamm *et al.*, “Live Imaging of Xwnt5A-ROR2 Complexes,” *PLoS One*, vol. 9, no. 10, p. e109428, Oct. 2014.
- [37] M. Luz *et al.*, “Dynamic Association with Donor Cell Filopodia and Lipid-Modification Are Essential Features of Wnt8a during Patterning of the Zebrafish Neuroectoderm,” *PLoS One*, vol. 9, no. 1, p. e84922, Jan. 2014.
- [38] S. Aldaz, L. M. Escudero, and M. Freeman, “Live imaging of Drosophila imaginal disc development,” *Proc Natl Acad Sci U S A*, vol. 107, no. 32, pp. 14217–14222, Aug. 2010.
- [39] A. C. Oates, N. Gorfinkiel, M. González-Gaitán, and C.-P. Heisenberg, “Quantitative approaches in developmental biology,” *Nat Rev Genet*, vol. 10, no. 8, pp. 517–530, Aug. 2009.
- [40] M. Mavrikis, O. Pourquie, and T. Lecuit, “Lighting up developmental mechanisms: how fluorescence imaging heralded a new era,” *Development*, vol. 137, no. 3, pp. 373–387, Jan. 2010.
- [41] P. Pantazis and W. Supatto, “Advances in whole-embryo imaging: a quantitative transition is underway,” *Nat Rev Mol Cell Biol*, vol. 15, no. 5, pp. 327–339, May 2014.
- [42] J. B. Gurdon, a Mitchell, and D. Mahony, “Direct and continuous assessment by cells of their position in a morphogen gradient,” *Nature*, vol. 376, no. 6540, pp. 520–521, 1995.
- [43] J. B. Gurdon and P. Y. Bourillot, “Morphogen gradient interpretation,” *Nature*, vol. 413, no. 6858, pp. 797–803, 2001.
- [44] S. J. Wharton, S. P. Basu, and H. L. Ashe, “Smad affinity can direct distinct readouts of the embryonic extracellular {D}pp gradient in *Drosophila*,” *Curr Biol*, vol. 14, no. 17, pp. 1550–1558, Sep. 2004.
- [45] J. Jaeger *et al.*, “Dynamic control of positional information in the early *Drosophila* embryo,” *Nature*, vol. 430, no. 6997, pp. 368–371, Jul. 2004.
- [46] G. T. Reeves, R. Kalifa, D. E. Klein, M. A. Lemmon, and S. Y. Shvartsman, “Computational analysis of EGFR inhibition by Argos,” *Dev. Biol.*, vol. 284, no. 2, pp. 523–535, Aug. 2005.
- [47] J. M. Dresch, M. A. Thompson, D. N. Arnosti, and C. Chiu, “Two-Layer Mathematical Modeling of Gene Expression: Incorporating DNA-Level Information and System Dynamics,” *SIAM J Appl Math*, vol. 73, no. 2, pp. 804–826, 2013.
- [48] R. Steward, “Dorsal, an embryonic polarity gene in *Drosophila*, is homologous to the vertebrate proto-oncogene, *c-rel*,” *Science (80-)*, vol. 238, no. 4827, pp. 692–694, Oct. 1987.
- [49] R. Steward, S. B. Zusman, L. H. Huang, and P. Schedl, “The dorsal protein is distributed in a gradient in early *Drosophila* embryos,” *Cell*, vol. 55, no. 3, pp. 487–495, Nov. 1988.
- [50] M. P. Belvin and K. V. Anderson, “A CONSERVED SIGNALING PATHWAY: The *Drosophila* Toll-Dorsal Pathway,” *Annu. Rev. Cell Dev. Biol.*, vol. 12, no. 1, pp. 393–416, Nov. 1996.
- [51] K. V Anderson, G. Jürgens, and C. Nüsslein-Volhard, “Establishment of dorsal-ventral polarity in the *Drosophila* embryo: Genetic studies on the role of the Toll gene product,” *Cell*, vol. 42, no. 3, pp. 779–789, Oct. 1985.
- [52] K. V Anderson, L. Bokla, and C. Nüsslein-Volhard, “Establishment of dorsal-ventral polarity in the *Drosophila* embryo: the induction of polarity by the Toll gene product,” *Cell*, vol. 42, no. 3, pp. 791–798, Oct. 1985.
- [53] R. Geisler, A. Bergmann, Y. Hiromi, and C. Nüsslein-Volhard, “*cactus*, a gene involved in dorsoventral pattern formation of *Drosophila*, is related to the I kappa B gene family of

- vertebrates.," *Cell*, vol. 71, no. 4, pp. 613–621, Nov. 1992.
- [54] S. Kidd, "Characterization of the *Drosophila* cactus locus and analysis of interactions between cactus and dorsal proteins.," *Cell*, vol. 71, no. 4, pp. 623–35, Nov. 1992.
- [55] M. P. Belvin, Y. Jin, and K. V Anderson, "Cactus protein degradation mediates *Drosophila* dorsal-ventral signaling.," *Genes Dev*, vol. 9, no. 7, pp. 783–793, Apr. 1995.
- [56] M. Reach, R. L. Galindo, P. Towb, J. L. Allen, M. Karin, and S. A. Wasserman, "A gradient of cactus protein degradation establishes dorsoventral polarity in the *Drosophila* embryo.," *Dev. Biol.*, vol. 180, no. 1, pp. 353–364, Nov. 1996.
- [57] A. M. Whalen and R. Steward, "Dissociation of the Dorsal-Cactus complex and phosphorylation of the Dorsal protein correlate with the nuclear localization of Dorsal.," *J Cell Biol*, vol. 123, no. 3, pp. 523–534, Nov. 1993.
- [58] J. Daigneault, L. Klemetsaune, and S. A. Wasserman, "The IRAK homolog Pelle is the functional counterpart of I κ B kinase in the *Drosophila* Toll pathway.," *PLoS One*, vol. 8, no. 9, p. e75150, 2013.
- [59] A. Stathopoulos and M. Levine, "Whole-genome analysis of *Drosophila* gastrulation.," *Curr. Opin. Genet. Dev.*, vol. 14, no. 5, pp. 477–484, Oct. 2004.
- [60] V. S. Chopra and M. Levine, "Combinatorial patterning mechanisms in the *Drosophila* embryo.," *Brief. Funct. Genomic. Proteomic.*, vol. 8, no. 4, pp. 243–9, Jul. 2009.
- [61] A. Stathopoulos and M. Levine, "Dorsal gradient networks in the *Drosophila* embryo.," *Dev. Biol.*, vol. 246, no. 1, pp. 57–67, Jun. 2002.
- [62] B. Moussian and S. Roth, "Dorsoventral axis formation in the *Drosophila* embryo--shaping and transducing a morphogen gradient," *Curr. Biol.*, vol. 15, no. 21, pp. R887--R899, Nov. 2005.
- [63] E. a Drier, L. H. Huang, and R. Steward, "Nuclear import of the *Drosophila* Rel protein Dorsal is regulated by phosphorylation.," *Genes Dev.*, vol. 13, no. 5, pp. 556–68, Mar. 1999.
- [64] E. A. Drier, S. Govind, and R. Steward, "Cactus-independent regulation of Dorsal nuclear import by the ventral signal," *Curr. Biol.*, vol. 10, no. 1, pp. 23–26, Jan. 2000.
- [65] S. K. H. Gillespie and S. A. Wasserman, "dorsal , a *Drosophila* Rel-Like Protein , Is Phosphorylated upon Activation of the Transmembrane Protein Toll," *Reactions*, vol. 14, no. 6, pp. 3559–3568, 1994.
- [66] S. Roth, Y. Hiromi, D. Godt, and C. Nüsslein-Volhard, "cactus, a maternal gene required for proper formation of the dorsoventral morphogen gradient in *Drosophila* embryos.," *Development*, vol. 112, no. 2, pp. 371–388, Jun. 1991.
- [67] M. A. Cardoso, M. Fontenele, B. Lim, P. M. Bisch, S. Y. Shvartsman, and H. M. Araujo, "A novel function for the I κ B inhibitor Cactus in promoting Dorsal nuclear localization and activity in the *Drosophila* embryo," *Development*, vol. 144, no. 16, pp. 2907–2913, Aug. 2017.
- [68] S. N. Carrell, M. D. O'Connell, T. Jacobsen, A. E. Pomeroy, S. M. Hayes, and G. T. Reeves, "A facilitated diffusion mechanism establishes the *Drosophila* Dorsal gradient," *Development*, vol. 144, no. 23, pp. 4450–4461, Dec. 2017.
- [69] M. D. O'Connell and G. T. Reeves, "The Presence of Nuclear Cactus in the Early *Drosophila* Embryo May Extend the Dynamic Range of the Dorsal Gradient," *PLoS Comput. Biol.*, vol. 11, no. 4, p. e1004159, 2015.
- [70] M. A. Digman and E. Gratton, "Imaging barriers to diffusion by pair correlation functions.," *Biophys J*, vol. 97, no. 2, pp. 665–673, Jul. 2009.

- [71] E. Hinde, F. Cardarelli, M. A. Digman, and E. Gratton, "In vivo pair correlation analysis of EGFP intranuclear diffusion reveals DNA-dependent molecular flow.," *Proc Natl Acad Sci U S A*, vol. 107, no. 38, pp. 16560–16565, Sep. 2010.
- [72] D. S. Schneider, K. L. Hudson, T. Y. Lin, and K. V Anderson, "Dominant and recessive mutations define functional domains of Toll, a transmembrane protein required for dorsal-ventral polarity in the Drosophila embryo.," *Genes Dev.*, vol. 5, no. 5, pp. 797–807, May 1991.
- [73] M. A. Digman, P. W. Wiseman, A. R. Horwitz, and E. Gratton, "Detecting protein complexes in living cells from laser scanning confocal image sequences by the cross correlation raster image spectroscopy method.," *Biophys J*, vol. 96, no. 2, pp. 707–716, Jan. 2009.
- [74] G. Hall, J. D. Hasday, and T. B. Rogers, "Regulating the regulator: NF- κ B signaling in heart," *J. Mol. Cell. Cardiol.*, vol. 41, no. 4, pp. 580–591, Oct. 2006.
- [75] O. Krichevsky and G. Bonnet, "Fluorescence correlation spectroscopy: the technique and its applications," *Reports Prog. Phys.*, vol. 65, no. 2, pp. 251–297, Jan. 2002.
- [76] K. M. Berland, P. T. So, Y. Chen, W. W. Mantulin, and E. Gratton, "Scanning two-photon fluctuation correlation spectroscopy: particle counting measurements for detection of molecular aggregation.," *Biophys. J.*, vol. 71, no. 1, pp. 410–420, 1996.
- [77] M. a Digman, R. Dalal, A. F. Horwitz, and E. Gratton, "Mapping the number of molecules and brightness in the laser scanning microscope.," *Biophys. J.*, vol. 94, no. 6, pp. 2320–32, Mar. 2008.

APPENDICES

Appendix S

Derivation of integral formula to calculate autocorrelation function of any arbitrary set of reaction/diffusion PDEs in single-point FCS

To derive the integral formula to calculate the autocorrelation function of raster scanning fluctuation spectroscopy, such as RICS, we first derive the formula for the autocorrelation function for fixed point FCS. This FCS derivation is also given in an alternate form in [75]. Consider a set of partial differential equations of the following form:

$$\frac{\partial \mathbf{c}}{\partial t} = D\nabla^2 \mathbf{c} + \mathbf{f}(\mathbf{c}), \quad (\text{S1})$$

where the $N \times 1$ column vector, \mathbf{c} , represents the state variables of the system (some or all of which are fluorescent), D represents an $N \times N$ diagonal matrix in which the diffusivity of state variable c_i is the i^{th} diagonal element of D , and $N \times 1$ column vector \mathbf{f} is a continuously differentiable, non-linear function of the state variables. Consider the steady state solution to this set of PDEs to be $\bar{\mathbf{c}}$. The fluctuations $\delta \mathbf{c}$ about that average, steady state value, due to particular micro-level rearrangements of molecules, are governed by:

$$\frac{\partial \delta \mathbf{c}}{\partial t} = D\nabla^2 \delta \mathbf{c} + \mathbf{J}(\bar{\mathbf{c}})\delta \mathbf{c}, \quad (\text{S2})$$

where $\mathbf{J}(\bar{\mathbf{c}})$ is the Jacobian matrix evaluated at the steady state $\bar{\mathbf{c}}$. Equation (2) can be reduced to a set of ODEs by applying a set of Fourier transforms (one for each spatial direction):

$$\frac{d\delta \tilde{\mathbf{c}}}{dt} = -\mathbf{q}^2 D \delta \tilde{\mathbf{c}} + \mathbf{J}(\bar{\mathbf{c}})\delta \tilde{\mathbf{c}} = \mathbf{A} \delta \tilde{\mathbf{c}}, \quad (\text{S3})$$

where $\delta \tilde{\mathbf{c}}$ is the Fourier transform of $\delta \mathbf{c}$, $\mathbf{A} \equiv -\mathbf{q}^2 D + \mathbf{J}(\bar{\mathbf{c}})$, and $\mathbf{q} \equiv [q_x \quad q_y \quad q_z]^T$. In this notation, q_x, q_y, q_z are the Fourier variables that replace the Cartesian variables x, y, z , respectively. The solution to this system of ODEs is:

$$\delta \tilde{\mathbf{c}}(\mathbf{q}, t) = \exp(t\mathbf{A}(\mathbf{q})) \delta \tilde{\mathbf{c}}(\mathbf{q}, 0) = \mathbf{V}(\mathbf{q})\mathbf{E}(\mathbf{q}, t)\mathbf{V}(\mathbf{q})^{-1} \delta \tilde{\mathbf{c}}(\mathbf{q}, 0), \quad (\text{S4})$$

where \mathbf{V} is the matrix of resulting from concatenating the column eigenvectors of \mathbf{A} , \mathbf{E} is an $N \times N$ diagonal matrix with $\exp(\lambda_i t)$ as the i^{th} element, and λ_i is the i^{th} eigenvalue of \mathbf{A} . Note that λ_i must correspond to the eigenvector in the i^{th} column of \mathbf{V} . Also note that the dependencies on t and \mathbf{q} have been made explicit.

The system is subjected to illumination by a focused laser, with excitation density given by $I(\mathbf{r})$. This results in the collection of $n(t)$ photons. In reality, this quantity n is discrete in time, as photon counting mechanisms collect photons over sampling time Δt . The photon count at time t is [75]:

$$n(t) = \Delta t \int d\mathbf{r} I(\mathbf{r}) \mathbf{Q}^T \mathbf{c}, \quad (\text{S5})$$

where \mathbf{Q} is a column vector in which element i is a measure of the fluorescence emission efficiency of molecular species i . Similarly, the fluctuations, δn , about the mean photon count, \bar{n} , are given by Equation (5), with $\delta \mathbf{c}$ substituted for \mathbf{c} , and \bar{n} is given by Equation (S5), but with $\bar{\mathbf{c}}$ substituted for \mathbf{c} .

Under these conditions, the autocorrelation function is given by [75]:

$$G(t) = \frac{(\Delta t)^2}{\bar{n}^2} \int \int d\mathbf{r} d\mathbf{r}' \langle I(\mathbf{r}) \mathbf{Q}^T \delta \mathbf{c}(\mathbf{r}, 0) I(\mathbf{r}') \mathbf{Q}^T \delta \mathbf{c}(\mathbf{r}', t) \rangle, \quad (\text{S6})$$

where the angle brackets indicate ensemble average. In Equation (S6), note that $I(\mathbf{r})$ and \mathbf{Q} are time independent, that the product $\mathbf{Q}^T \delta \mathbf{c}$ is a scalar, and therefore $\mathbf{Q}^T \delta \mathbf{c} = \mathbf{Q} \delta \mathbf{c}^T$. Using these properties, Equation (S6) can be rearranged to:

$$G(t) = \frac{(\Delta t)^2}{\bar{n}^2} \int \int d\mathbf{r} d\mathbf{r}' I(\mathbf{r}) I(\mathbf{r}') \mathbf{Q}^T \langle \delta \mathbf{c}(\mathbf{r}', t) \delta \mathbf{c}(\mathbf{r}, 0)^T \rangle \mathbf{Q}, \quad (\text{S7})$$

To evaluate this integral, we will focus on evaluation of the factors in angle brackets. If we apply the set of Fourier transforms to $\delta \mathbf{c}(\mathbf{r}', t)$, we arrive at:

$$\begin{aligned} \delta \mathbf{c}(\mathbf{r}', t) &= \mathfrak{F}^{-1}[\mathfrak{F}[\delta \mathbf{c}(\mathbf{r}', t)]] = \mathfrak{F}^{-1}[\delta \tilde{\mathbf{c}}(\mathbf{q}, t)] = \mathfrak{F}^{-1}[\text{VEV}^{-1} \delta \tilde{\mathbf{c}}(\mathbf{q}, 0)] \\ &= (2\pi)^{-3/2} \int d\mathbf{q} e^{-i\mathbf{q}\cdot\mathbf{r}'} \text{VEV}^{-1} \delta \tilde{\mathbf{c}}(\mathbf{q}, 0), \end{aligned} \quad (\text{S8})$$

where V and E have been defined previously. As the Fourier transform operators can exchange with the ensemble average operators, this implies:

$$\langle \delta \mathbf{c}(\mathbf{r}', t) \delta \mathbf{c}(\mathbf{r}, 0)^T \rangle = (2\pi)^{-3/2} \int d\mathbf{q} e^{-i\mathbf{q}\cdot\mathbf{r}'} \text{VEV}^{-1} \langle \delta \tilde{\mathbf{c}}(\mathbf{q}, 0) \delta \mathbf{c}(\mathbf{r}, 0)^T \rangle, \quad (\text{S9})$$

In a similar fashion, the initial conditions of the Fourier-space fluctuation, $\delta \tilde{\mathbf{c}}$, can be expressed as the Fourier transform of the initial conditions of the Cartesian-space fluctuation:

$$\delta \tilde{\mathbf{c}}(\mathbf{q}, 0) = \mathfrak{F}[\delta \mathbf{c}(\mathbf{r}'', 0)] = (2\pi)^{-3/2} \int d\mathbf{r}'' e^{i\mathbf{q}\cdot\mathbf{r}''} \delta \mathbf{c}(\mathbf{r}'', 0). \quad (\text{S10})$$

Substituting Equation (S10) into (S9):

$$\langle \delta \mathbf{c}(\mathbf{r}', t) \delta \mathbf{c}(\mathbf{r}, 0)^T \rangle = (2\pi)^{-3} \int d\mathbf{q} e^{-i\mathbf{q}\cdot\mathbf{r}'} \int d\mathbf{r}'' e^{i\mathbf{q}\cdot\mathbf{r}''} \text{VEV}^{-1} \langle \delta \tilde{\mathbf{c}}(\mathbf{r}'', 0) \delta \mathbf{c}(\mathbf{r}, 0)^T \rangle, \quad (\text{S11})$$

Now note that the two factors inside the angle brackets are both vectors; the first is a column vector, while the second is a row vector. The multiplication of these two results in an $N \times N$ matrix in which the element on the i^{th} row, j^{th} column is $\delta c_i(\mathbf{r}'', 0) \delta c_j(\mathbf{r}, 0)$. However, the correlation of two species at two locations, with a delay time of zero, is zero unless it is the same species at the same location. In other words [75]:

$$\langle \delta \tilde{\mathbf{c}}(\mathbf{r}'', 0) \delta \mathbf{c}(\mathbf{r}, 0)^T \rangle = \langle \delta \tilde{\mathbf{c}}(\mathbf{r}'', 0) \delta \mathbf{c}(\mathbf{r}, 0)^T \rangle = \bar{\mathbf{C}} \delta(\mathbf{r} - \mathbf{r}''), \quad (\text{S12})$$

where $\bar{\mathbf{c}}$ is an $N \times N$ diagonal matrix with the elements of $\bar{\mathbf{c}}$ on the diagonals, and the δ denotes the Dirac delta function, and does not indicate a fluctuation variable as in other contexts.

Substituting Equation (S12) into (S11) gives:

$$\begin{aligned} \langle \delta \mathbf{c}(\mathbf{r}', t) \delta \mathbf{c}(\mathbf{r}, 0)^T \rangle &= (2\pi)^{-3} \int d\mathbf{q} e^{-i\mathbf{q}\cdot\mathbf{r}'} \int d\mathbf{r}'' e^{i\mathbf{q}\cdot\mathbf{r}''} \text{VEV}^{-1} \bar{\mathbf{c}} \delta(\mathbf{r} - \mathbf{r}'') \\ &= (2\pi)^{-3} \int d\mathbf{q} e^{-i\mathbf{q}\cdot\mathbf{r}'} e^{i\mathbf{q}\cdot\mathbf{r}} \text{VEV}^{-1} \bar{\mathbf{c}}. \end{aligned} \quad (\text{S13})$$

Finally, we substitute Equation (S13) into (S7):

$$G(t) = \frac{(\Delta t)^2}{\bar{n}^2} (2\pi)^{-3} \int \int d\mathbf{r} d\mathbf{r}' I(\mathbf{r}) I(\mathbf{r}') \int d\mathbf{q} \mathbf{Q}^T \text{VEV}^{-1} \bar{\mathbf{c}} \mathbf{Q} e^{-i\mathbf{q}\cdot\mathbf{r}'} e^{i\mathbf{q}\cdot\mathbf{r}}. \quad (\text{S14})$$

Now, if we exchange the order of integration, and collect all factors that do not depend on \mathbf{r} or \mathbf{r}' outside of the integrals for those spatial variables, we get:

$$G(t) = \frac{(\Delta t)^2}{\bar{n}^2} (2\pi)^{-3} \int d\mathbf{q} \mathbf{Q}^T \text{VEV}^{-1} \bar{\mathbf{c}} \mathbf{Q} \int \int d\mathbf{r} d\mathbf{r}' I(\mathbf{r}) I(\mathbf{r}') e^{-i\mathbf{q}\cdot\mathbf{r}'} e^{i\mathbf{q}\cdot\mathbf{r}}. \quad (\text{S15})$$

At this point, the two integrals in \mathbf{r} and \mathbf{r}' can be separated from each other, which results in what amounts to two Fourier transforms of the excitation density function, $I(\mathbf{r})$:

$$G(t) = \frac{(\Delta t)^2}{\bar{n}^2} \int d\mathbf{q} \mathbf{Q}^T \text{VEV}^{-1} \bar{\mathbf{c}} \mathbf{Q} \left[(2\pi)^{-3/2} \int d\mathbf{r} I(\mathbf{r}) e^{i\mathbf{q}\cdot\mathbf{r}} \right] \left[(2\pi)^{-3/2} \int d\mathbf{r}' I(\mathbf{r}') e^{-i\mathbf{q}\cdot\mathbf{r}'} \right]. \quad (\text{S16})$$

Now, $I(\mathbf{r})$ is typically taken to be a triple Gaussian:

$$I(\mathbf{r}) = I_0 \exp\left(-\frac{2(x^2 + y^2)}{w_0^2} - \frac{2z^2}{w_z^2}\right), \quad (\text{S17})$$

where w_0 is a measure of the spatial extent of the excitation density in the xy plane (usually taken to be the radius of the first local minimum in the point spread function), and w_z is that along the axial (z) direction. The Gaussian approximation to the excitation density is useful, as it has a very tractable Fourier transform:

$$\tilde{I}(\mathbf{q}) = \frac{I_0 w_0^2 w_z}{8} \exp\left(-\frac{w_0^2}{8} (q_x^2 + q_y^2) - \frac{w_z^2}{8} q_z^2\right). \quad (\text{S18})$$

This definition of $I(\mathbf{r})$ also allows us to further evaluate \bar{n} :

$$\bar{n} = \Delta t \mathbf{Q}^T \bar{\mathbf{c}} I_0 w_0^2 w_z^2 \left(\frac{\pi}{2}\right)^{3/2}. \quad (\text{S19})$$

Substituting Equations (S18,S19) into (S16):

$$G(t) = \frac{1}{8\pi^3 (\mathbf{Q}^T \bar{\mathbf{c}})^2} \int d\mathbf{q} \exp\left(-\frac{w_0^2}{4} (q_x^2 + q_y^2) - \frac{w_z^2}{4} q_z^2\right) \mathbf{Q}^T \text{VEV}^{-1} \bar{\mathbf{c}} \mathbf{Q}. \quad (\text{S20})$$

This is the final form of the ACF for single-point FCS.

Derivation of integral formula to calculate autocorrelation function of any arbitrary set of reaction/diffusion PDEs in scanning FCS

The main difference between single-point FCS and scanning FCS methods (such as RICS) is that, in single-point FCS, the excitation density function, $I(\mathbf{r})$, is fixed, while in scanning FCS, its position changes with time. In the latter case, $I(\mathbf{r})$ is replaced with $I(\mathbf{r} - \mathbf{r}_s(t))$, where $\mathbf{r}_s(t) = [\xi(t)\Delta r \quad \eta(t)\Delta r]^T$ is the location of the center of the focused laser, which corresponds to the scanning. Here ξ and η are the x and y positions within the image, in pixel numbers, and Δr is the xy pixel size in microns. If the scanning is raster (as in RICS), then the positions $\xi(t)$ and $\eta(t)$ are implicitly given by $t = \tau_p \xi + \tau_l \eta$ and $\xi \in \{1, 2, \dots, W\}$, where τ_p and τ_l are the pixel dwell time and the line scan time, respectively, and W is the pixel width of the image. Given this change to the excitation density, Equation (S7) becomes:

$$G_s(t) = \frac{(\Delta t)^2}{\bar{n}^2} \int \int d\mathbf{r} d\mathbf{r}' I(\mathbf{r} - \mathbf{r}_s(0)) I(\mathbf{r}' - \mathbf{r}_s(t)) \mathbf{Q}^T \langle \delta \mathbf{c}(\mathbf{r}', t) \delta \mathbf{c}(\mathbf{r}, 0)^T \rangle \mathbf{Q}, \quad (\text{S21})$$

where the “s” subscript on $G_s(t)$ denotes the scanning ACF. At this point, one may perform a change of variables to a new coordinate system always centered on the excitation density function. In that case, an equivalent formulation is [76]:

$$G_s(t) = \frac{(\Delta t)^2}{\bar{n}^2} \int \int d\mathbf{r} d\mathbf{r}' I(\mathbf{r}) I(\mathbf{r}') \mathbf{Q}^T \langle \delta \mathbf{c}(\mathbf{r}' - \mathbf{r}_s(t), t) \delta \mathbf{c}(\mathbf{r} - \mathbf{r}_s(0), 0)^T \rangle \mathbf{Q}. \quad (\text{S22})$$

The derivation proceeds with every \mathbf{r} outside of $I(\mathbf{r})$ replaced with $\mathbf{r} - \mathbf{r}_s(0)$, and every \mathbf{r}' outside of $I(\mathbf{r}')$ replaced with $\mathbf{r}' - \mathbf{r}_s(t)$ up until and including Equation (S15), whose analog is below:

$$G_s(t) = \frac{(\Delta t)^2}{\bar{n}^2} (2\pi)^{-3} \int d\mathbf{q} \mathbf{Q}^T \text{VEV}^{-1} \bar{\mathbf{C}} \mathbf{Q} \int \int d\mathbf{r} d\mathbf{r}' I(\mathbf{r}) I(\mathbf{r}') e^{-i\mathbf{q} \cdot (\mathbf{r}' - \mathbf{r}_s(t))} e^{i\mathbf{q} \cdot (\mathbf{r} - \mathbf{r}_s(0))}. \quad (\text{S23})$$

The next step, found in Equation (S16), was to group the factors containing \mathbf{r} together, and the factors containing \mathbf{r}' together, which resulted in two Fourier transforms of the excitation density profile. The same step is considered here, except the \mathbf{r}_s components are factored out of the exponentials to create the proper Fourier transforms of the excitation profiles:

$$G_s(t) = \frac{(\Delta t)^2}{\bar{n}^2} \int d\mathbf{q} e^{i\mathbf{q} \cdot (\mathbf{r}_s(t) - \mathbf{r}_s(0))} \mathbf{Q}^T \text{VEV}^{-1} \bar{\mathbf{C}} \mathbf{Q} \left[(2\pi)^{-3/2} \int d\mathbf{r} I(\mathbf{r}) e^{i\mathbf{q} \cdot \mathbf{r}} \right] \left[(2\pi)^{-3/2} \int d\mathbf{r}' I(\mathbf{r}') e^{-i\mathbf{q} \cdot \mathbf{r}'} \right]. \quad (\text{S24})$$

From here, the only difference between the single-point and scanning FCS cases is the exponential factor, $\exp(i\mathbf{q} \cdot (\mathbf{r}_s(t) - \mathbf{r}_s(0)))$. Therefore, the analogy to Equation (S20) becomes:

$$G_s(t) = \frac{1}{8\pi^3(\mathbf{Q}^T \bar{\mathbf{c}})^2} \int d\mathbf{q} e^{i\mathbf{q} \cdot (\mathbf{r}_s(t) - \mathbf{r}_s(0))} \exp\left(-\frac{w_0^2}{4}(q_x^2 + q_y^2) - \frac{w_z^2}{4}q_z^2\right) \mathbf{Q}^T \text{VEV}^{-1} \bar{\mathbf{C}} \mathbf{Q}. \quad (\text{S25})$$

Now note that the VEV^{-1} factor arises from the eigenvalues and eigenvectors of $\mathbf{A}(\mathbf{q})$, and the only dependence of \mathbf{A} on \mathbf{q} is through \mathbf{q}^2 . Therefore, VEV^{-1} is an even function of \mathbf{q} , as is the Gaussian factor. If we split the imaginary exponential into odd (imaginary) and even (real) parts:

$$\exp\left(i\mathbf{q} \cdot (\mathbf{r}_s(t) - \mathbf{r}_s(0))\right) = \cos\left(\mathbf{q} \cdot (\mathbf{r}_s(t) - \mathbf{r}_s(0))\right) + i \sin\left(\mathbf{q} \cdot (\mathbf{r}_s(t) - \mathbf{r}_s(0))\right), \quad (\text{S26})$$

then we find that the imaginary part integrates to zero, as it is an odd function times two even functions, integrated over all space. Therefore, our final formula for the scanning ACF becomes:

$$G_s(t) = \frac{1}{8\pi^3(\mathbf{Q}^T \bar{\mathbf{c}})^2} \int d\mathbf{q} \cos\left(\mathbf{q} \cdot (\mathbf{r}_s(t) - \mathbf{r}_s(0))\right) \exp\left(-\frac{w_0^2}{4}(q_x^2 + q_y^2) - \frac{w_z^2}{4}q_z^2\right) \mathbf{Q}^T \text{VEV}^{-1} \bar{\mathbf{C}} \mathbf{Q}. \quad (\text{S27})$$

A Two-Component Model with One Diffusible Species and One Non-Diffusible Species

Here we describe the derivation of the two-component model that is used in Figures 2.4 and S4. In this two-component model, it is assumed DI present in the nucleus can be in two states: free or DNA bound. The DNA-bound DI is assumed to be immobile. We assume the nucleus is spherical with radius R and with radial symmetry. We assume DI/Cact complex and Cact are present in the nucleus in negligible amounts. We also assume that free DNA sites are in excess, so that $[DNA] \approx [DNA]_{tot} = \text{a constant}$. Therefore, the equations are as follows:

$$\frac{\partial [DI]}{\partial t} = D \frac{1}{r^2} \frac{\partial}{\partial r} \left(r^2 \frac{\partial [DI]}{\partial r} \right) - k'_{on}[DI] + k_{off}B, \quad (\text{S28})$$

$$\frac{\partial B}{\partial t} = k'_{on}[DI] - k_{off}B, \quad (\text{S29})$$

where $[DI]$ and B are the concentrations of free DI-GFP and DI-GFP/DNA complex, respectively, and $k'_{on} = k_{on}[DNA]$. The parameters k_{on} and k_{off} are the rate constants of DI binding to and dissociating from the DNA, respectively. The parameter D is the diffusivity of DI-GFP.

$[DI]$ has the following boundary conditions:

$$\left. \frac{\partial [DI]}{\partial r} \right|_{r=0} = 0, \quad -D \left. \frac{\partial [DI]}{\partial r} \right|_{r=R} = k_{in,DI}[DI]_{cyt} - k_{out,DI}[DI]|_{r=R}, \quad (\text{S30})$$

where $[DI]_{cyt}$ is the local cytoplasmic concentration of DI (assumed constant), and $k_{in,DI}$ and $k_{out,DI}$ are the nuclear import and export rates of DI, respectively. It should be noted that, at steady state, Equations (1-3) admit a uniform solution to all species, in which DI/DNA binding

and nuclear import/export are all in equilibrium. In our RICS analysis, we assume we are operating in this regime. The steady state solutions depend on the equilibrium constants $K_{DNA} = k'_{on}/k_{off}$ and $K_{nuc,DI} = k_{in,DI}/k_{out,DI}$:

$$\overline{[DI]} = K_{nuc,DI}[DI]_{cyt}, \quad \overline{B} = K_{DNA}\overline{[DI]}, \quad (S31)$$

where the overbars indicate steady state values. Therefore, the vector $\bar{\mathbf{c}}$ is given by:

$$\bar{\mathbf{c}} = K_{nuc,DI}[DI]_{cyt} * [1 \quad K_{DNA}]^T. \quad (S32)$$

These equations are linear, and therefore, the fluctuation terms of DI and DI/DNA ($\delta[DI]$ and δB , respectively) are as follows:

$$\frac{\partial \delta[DI]}{\partial t} = D \nabla^2 \delta[DI] - k'_{on} \delta[DI] + k_{off} \delta B, \quad (S33)$$

$$\frac{\partial \delta B}{\partial t} = k'_{on} \delta[DI] - k_{off} \delta B, \quad (S34)$$

From this formulation, the matrices D and J are:

$$D = \begin{bmatrix} D & 0 \\ 0 & 0 \end{bmatrix}, \quad J = \begin{bmatrix} -k'_{on} & k_{off} \\ k'_{on} & -k_{off} \end{bmatrix}. \quad (S35)$$

We also assume that DI-GFP is able to fluoresce equally well either free or DNA bound, in which case, $\mathbf{Q} = [1 \quad 1]^T$.

If the values of k'_{on} or k_{off} are unknown, then one may study the how the binding affinity between DI and the DNA affects the ACF. In this case, the fraction of DI that is free (i.e., not bound to the DNA) is:

$$\phi = \frac{\overline{[DI]}}{\overline{[DI]} + \overline{B}} = \frac{1}{1 + K_{DNA}} = \frac{1}{1 + k'_{on}/k_{off}}. \quad (S36)$$

In our simulated two-component systems (Figures 2.4B,C and S4), we assumed $D = 2.3 \mu\text{m}^2/\text{s}$, which is the average value of the diffusivity from all of our cytoplasmic RICS measurements, and $k_{off} = 0.0025 \text{ s}^{-1}$ (see below for justification). We varied ϕ between zero and one, so that K_{DNA} (and thus, $k'_{on} = k_{off}K_{DNA}$) varied between (near) infinity and zero. For each choice of ϕ , we calculated the ACF resulting from the simulated two-component system and fit one-component systems to the two-component ACFs, which resulted in a one-component diffusivity estimate.

When we fit our two-component model to our RICS data, we once again set $D = 2.3 \mu\text{m}^2/\text{s}$, k_{off} equal to 0.0025 s^{-1} , and allowed k'_{on} to vary between 10^{-4} and 1000. We avoided fitting multiple biophysical parameters simultaneously to avoid overfitting, which is a problem that we have observed in other RICS applications in our lab (not shown).

A Three-Component Model of DI/Cact/DNA interactions

A three-component model that tracks the nuclear concentrations of DI, Cact, DI/Cact complex, DNA, and DI/DNA complex, was formulated. We adopt the same assumptions as laid out above, except here we assume DI/Cact complex is present in the nuclei in non-negligible amounts. (We still assume Cact is present in the nucleus in negligible amounts). Additionally, we assume that DI and DI/Cact complex have roughly the same diffusivity, D , and that the rate of DI/Cact complex dissociation is negligible, as Toll signaling is absent from the nucleus. Therefore, in addition to Equations (S28-S30), this model also includes the following equation and boundary conditions for DI/Cact complex:

$$\frac{\partial[DC]}{\partial t} = D \frac{1}{r^2} \frac{\partial}{\partial r} \left(r^2 \frac{\partial[DC]}{\partial r} \right), \quad (\text{S37})$$

$$\left. \frac{\partial[DC]}{\partial r} \right|_{r=0} = 0, \quad -D \left. \frac{\partial[DC]}{\partial r} \right|_{r=R} = k_{in,DC}[DC]_{cyt} - k_{out,DC}[DC]|_{r=R}, \quad (\text{S38})$$

where $[DC]$ is the concentration of DI-GFP/Cact complex in the nucleus, $[DC]_{cyt}$ is the local cytoplasmic concentration of species DI/Cact complex (assumed constant), and $k_{in,DC}$ and $k_{out,DC}$ are the nuclear import and export rates of species DI/Cact complex, respectively. As before, at steady state, Equations (S28-S30,S37,S38) admit a uniform solution to all species. The steady state solutions, which are given in Equation (S31) and as $\overline{[DC]} = K_{nuc,DC}[DC]_{cyt}$, depend on the equilibrium constants $K_{DNA} = k'_{on}/k_{off}$, $K_{nuc,DI} = k_{in,DI}/k_{out,DI}$, and $K_{nuc,DC} = k_{in,DC}/k_{out,DC}$.

Therefore, the vector $\bar{\mathbf{c}}$ is given by:

$$\bar{\mathbf{c}} = [\overline{[DI]} \quad \bar{B} \quad \overline{[DC]}]^T = [K_{nuc,DI}[DI]_{cyt} \quad K_{DNA}K_{nuc,DI}[DI]_{cyt} \quad K_{nuc,DC}[DC]_{cyt}]^T. \quad (\text{S39})$$

The fluctuation terms of DI and DI/DNA were previously given in Equations (33-34). The fluctuation of DI/Cact complex is given by:

$$\frac{\partial \delta[DC]}{\partial t} = D \nabla^2 \delta[DC]. \quad (\text{S40})$$

From this formulation, the matrices D and J are:

$$D = \begin{bmatrix} D & 0 & 0 \\ 0 & 0 & 0 \\ 0 & 0 & D \end{bmatrix}, \quad J = \begin{bmatrix} -k'_{on} & k_{off} & 0 \\ k'_{on} & -k_{off} & 0 \\ 0 & 0 & 0 \end{bmatrix}. \quad (\text{S41})$$

As before, we assume that DI-GFP is able to fluoresce equally well either free or bound to DNA or Cact, in which case, $\mathbf{Q} = [1 \quad 1 \quad 1]^T$.

Under these conditions, there are two parameters that control the fraction of total DI (free DI + DI/Cact complex + DI/DNA): K_{DNA} , or, equivalently, ϕ , given by Equation (36), and ρ :

$$\rho \equiv \frac{K_{nuc,DC}[DC]_{cyt}}{K_{nuc,Dl}[Dl]_{cyt}}. \quad (S42)$$

The vector \bar{c} can thus be expressed as $\bar{c} = K_{nuc,Dl}[Dl]_{cyt} * [1 \quad K_{DNA} \quad \rho]^T$. In the real embryo, K_{DNA} is likely constant along the DV axis, as are $K_{nuc,DC}$ and $K_{nuc,Dl}$. The exception would be if Toll-mediated phosphorylation of Dl modified $k_{in,Dl}$ or $k_{out,Dl}$ (see, for example, Whalen and Steward, 1993 and Drier et al., 1999, 2000). On the other hand, ρ varies strongly with DV position due to a varying ratio of $[DC]_{cyt}/[Dl]_{cyt}$. Therefore, the three component model would predict that the apparent diffusivity of Dl is dependent on ρ (or, equivalently, χ ; see Equation (S44) below).

When we fit this model to our RICS data, we set $k'_{on} = 0.01 \text{ s}^{-1}$, $\phi = 0.2$, which corresponds to $K_{DNA} = 4$, and thus, $k_{off} = 0.0025 \text{ s}^{-1}$, and we allowed ρ to be the only variable parameter. Bounds on ρ were set to be 10^{-4} to 1000.

$k'_{on} = 0.01 \text{ s}^{-1}$ was chosen for the following reason. First, mass transfer arguments suggest that values of k_{on} fall between 10^5 and $10^6 \text{ M}^{-1} \text{ s}^{-1}$. Next, we assumed 10^4 DNA sites for Dl to bind to. If we count these DNA sites as continuously scattered throughout the nucleus, which has a diameter of roughly 5 microns, then $k'_{on} = k_{on} \times 10^4 / V_{nucleus} \approx 0.01 \text{ s}^{-1}$. $\phi = 0.2$ was chosen because it is roughly the average value of ϕ in our two-component model fit to the RICS data sets in which the nuclear diffusivity of the one-component model was less than $0.1 \mu\text{m}^2/\text{s}$ (see Fig 4E). As described in the previous section, we avoided fitting multiple biophysical parameters simultaneously to avoid overfitting.

Reduction of the Three-Component Dl/Cact/DNA Model into a Two-Component Model

The three-component model that was introduced previously can be simplified to a two component model, which we call the “reduced model”. The reduced model is equivalent to the original two-component model (Figure 2.4A), which was used in Fig. 4, but has a more natural biophysical interpretation than the original two-component model. In particular, in the original two-component model, one had to assume that the affinity of Dl for DNA binding varied along the DV axis, which is unlikely. However, in the reduced model, as can be seen below, it is the ratio of cytoplasmic concentrations of Dl/Cact complex and free Dl that varies along the DV axis, which is known to occur.

To reduce the three-component model to two components, we first add Equations (S28) and (S37) to produce:

$$\frac{\partial A}{\partial t} = D \frac{1}{r^2} \frac{\partial}{\partial r} \left(r^2 \frac{\partial A}{\partial r} \right) - k'_{on}[Dl] + k_{off}B, \quad (S43)$$

where A is defined as $[Dl] + [DC]$. If free Dl is just a fraction of A , then $[Dl] = \chi A$, where

$$\chi = \frac{[Dl]}{A} = \frac{[Dl]}{[Dl] + [DC]} = \frac{K_{eq,Dl}[Dl]_{cyt}}{K_{eq,Dl}[Dl]_{cyt} + K_{eq,DC}[DC]_{cyt}} = \frac{1}{1 + \rho}, \quad (S44)$$

where ρ is defined in Equation (S42). This converts Equation (S43) into:

$$\frac{\partial A}{\partial t} = D \frac{1}{r^2} \frac{\partial}{\partial r} \left(r^2 \frac{\partial A}{\partial r} \right) - \chi k'_{on} A + k_{off} B. \quad (\text{S45})$$

While this is a major simplification that ignores the dynamics of DI/Cact complex, if we use Equation (S45) to formulate the fluctuations in non-DNA-bound DI, δA , we arrive at:

$$\frac{\partial \delta A}{\partial t} = D \nabla^2 \delta A - \hat{k}_{on} \delta A + k_{off} \delta B, \quad (\text{S46})$$

where we have defined $\hat{k}_{on} \equiv \chi k'_{on}$. This equation is analogous to Equation (S33), and, along with Equation (S34), defines a system of fluctuation equations where the diffusion matrix and Jacobian are given by Equation (S35), with \hat{k}_{on} replacing k'_{on} . The vector $\bar{\mathbf{c}}$ becomes:

$$\bar{\mathbf{c}} = K_{nuc,DI}[DI]_{cyt} * [(1 + \rho) \quad K_{DNA}]^T, \quad (\text{S47})$$

where K_{DNA} is still defined as k'_{on}/k_{off} . If we divide $\bar{\mathbf{c}}$ by $1 + \rho$, we arrive at:

$$\begin{aligned} \bar{\mathbf{c}} &= K_{nuc,DI}[DI]_{cyt} * \left[1 \quad \frac{K_{DNA}}{1 + \rho} \right]^T = K_{nuc,DI}[DI]_{cyt} * [1 \quad \chi K_{DNA}]^T \\ &= K_{nuc,DI}[DI]_{cyt} * \left[1 \quad (\hat{k}_{on}/k_{off}) \right]^T, \end{aligned} \quad (\text{S48})$$

In the analysis of the two component model, the parameter ϕ was defined as the ratio between free DI and total DI (free + DNA-bound). Here, we define ϕ similarly: the ratio between non-DNA-bound DI (i.e., free + Cact-bound) and total DI (free + Cact-bound + DNA-bound). Thus, in the reduced model,

$$\phi = \frac{1 + \rho}{1 + \rho + K_{DNA}} = \frac{1}{1 + \frac{K_{DNA}}{1 + \rho}} = \frac{1}{1 + \chi K_{DNA}} = \frac{1}{1 + (\hat{k}_{on}/k_{off})}. \quad (\text{S49})$$

It can be seen that our reduced model is mathematically identical to our original two-component model, with \hat{k}_{on} replacing k'_{on} . However, the reduced model has an interpretive advantage over the original two component model in that it is natural for $\hat{k}_{on} = \chi k'_{on}$ to vary with position along the DV axis (due to variations in χ), but not necessarily K_{DNA} to do so:

$$\chi = \frac{1}{1 + \rho} = \frac{1}{1 + \left(\frac{K_{nuc,DC}[DC]_{cyt}}{K_{nuc,DI}[DI]_{cyt}} \right)}. \quad (\text{S50})$$

Raster Image Correlation Spectroscopy (RICS) analysis

Time series images consistent with RICS analysis were analyzed in the following way. Let I_0 be the 256×256 pixel DI-GFP channel frame at time point t_i . A background subtraction by I_{sw} , the

average of a sliding window with a five-frame radius, was performed to remove the effect of global movement of large structures [77]: $I_{bs} = I_0 - I_{sw}$. Next, the average intensity of every pixel in the sliding window, \bar{I}_{sw} , was added back to frame j to ensure the frame intensity was not near zero, to yield array $I = I_0 - I_{sw} + \bar{I}_{sw}$. Next, a fast Fourier transform of the frame was computed to yield the array $J = \mathcal{F}[I]$ in the Fourier domain. Next, an array g_j was computed as the inverse Fourier transform of J multiplied by its complex conjugate on an element-by-element basis: $g_j = JJ^*$. Finally, the autocorrelation function, G_j , for frame j was computed as $G_j = g_j / (HW\bar{I}^2) - 1$, where H and W are the original height and width of the image frame, and \bar{I} is the mean intensity of all pixels in I . The final autocorrelation function, G_s , was computed as the average of all G_j for $j = 1 \dots 200$. Cross-correlation functions were computed in a similar way, except J was multiplied by the complex conjugate of the Fourier transform of frame i from the background-subtracted H2A-RFP channel.

Due to the fact that photon shot noise is perfectly autocorrelated at position (0,0), the computed value of the autocorrelation function at position (0,0) is incorrect. Additionally, noise levels can also affect the value of G_s at position (1,0) (i.e., at $\xi = 1, \eta = 0$). Both of these pixels are interpolated by a quadratic with symmetry at $\xi = 0$ using the points at (2,0), (3,0), and (4,0).

This is the same procedure used in the simFCS software (Gratton, personal communication).

To find nuclear RICS, a nuclear mask for each frame j was found in the following manner. First, frames one through 200 were divided into 20 groups of ten frames each. In each group k , the ten frames were averaged to produce an average frame. This average frame of group k was eroded with a disk-shaped structuring element of one micron, dilated with a disk-shaped element of a half micron, then Gaussian blurred with a standard deviation of a half micron, which resulted in a frame called I_{EDG} .

Next, the frame I_{EDG} was saturated by 2% at both ends. In other words, the 2nd and 98th percentile intensities, i_2 and i_{98} , respectively, were found, and I_{EDG} was rescaled by:

$$I_{rs} = \frac{I_{EDG} - i_2}{i_{98} - i_2}$$

This resulted in a frame with 2% of its pixels less than zero, and 2% greater than one. These were set to zero and one, respectively.

Next, a global hard threshold was chosen based on the microscope zoom-level and time point (to account for possible bleaching of the H2A-RFP channel). If the pixel size was less than 0.05 microns, the threshold to determine the nuclei varied linearly between 0.30 for $k = 1$ and 0.15 for $k = 20$, while the threshold to determine the cytoplasm varied linearly between 0.1 for $k = 1$ and 0.05 for $k = 20$. If the pixel size was greater than 0.05 microns, the global thresholds were time invariant: 0.55 for nucleus, and 0.25 for cytoplasm.

After global thresholding, a hole-filling operation was performed on the nuclei, then the nuclei were eroded by 0.5 microns. The cytoplasm was also eroded by 0.5 microns. These erosion steps were to create a conservative estimate of nucleus vs cytoplasm. The nuclear or cytoplasmic mask for group k served as the mask for the frames that composed group k .

Once a nuclear mask image, I_{nuc} , was found for frame j , all pixels in the array I outside the mask are set to zero, yielding I_2 . Then array $g_{nuc,j}$ was computed similar to g_j , but using I_2 instead of I . Additionally, an array, D , analogous to $g_{nuc,j}$, was calculated using I_{nuc} instead of I_2 . Finally, the autocorrelation function for that frame and mask was calculated as $G_{nuc,j} =$

$g_j/(D\bar{I}_2^2) - 1$, where the division is on a pixel-by-pixel basis, and where \bar{I}_2 is the mean intensity of all pixels in I_2 within mask I_{nuc} . The final autocorrelation function, $G_{s,nuc}$, was computed as the average of all $G_{nuc,j}$ for $j = 1 \dots 200$. Cross correlation functions using a nuclear mask were computed in a similar way as described here and above, except \bar{I}_2 is replaced by the geometric mean of the mean intensities of I_2 and the corresponding H2A-RFP image.

To find cytoplasmic RICS, the same procedures are followed, except mask I_{cyt} is used instead of I_{nuc} .

Analysis of photobleaching time course images

The general procedure for image analysis of the FRAP experiments was outlined in the main text. Further detailed information can be found in (Carrell et al., 2017); here we described details of the segmentation of nuclei and of the fitting the fluorescence recovery curve to a differential equation model. These two procedures differ slightly from what was used in (Carrell et al., 2017). All images described below were converted from 16-bit arrays to double precision. To segment the nuclei, the first observation is that, after frame 1, the bleached nucleus in both the DI-GFP and H2A-RFP channels becomes bleached. This presented a challenge in segmenting the bleached nucleus in frames after frame 1. Therefore, to protect the identity of the bleached nucleus in the rest of the time course, the average of frames 2-10 were subtracted from frame 1, which resulted in a “difference frame” in which the bleached nucleus was the brightest object. The difference frame was then Gaussian blurred with standard deviation of a half micron, eroded with a disk-shaped structuring element of two microns, dilated with a disk-shaped element of a half micron, then blurred again with a standard deviation of a half micron. (Under normal circumstances, the first blurring would be unnecessary, but the process of subtracting by an average frame resulted in small, crescent-shaped artifacts that arose from when nuclei moved slightly.) This procedure removed artifacts from the image and resulted in a frame that further highlighted the bleached nucleus (hereafter referred to as I_{bn}).

The nuclei were segmented in the following way. First, frame j was eroded with a disk-shaped structuring element of two microns, dilated with a disk-shaped element of a half micron, then Gaussian blurred with a standard deviation of a half micron, which resulted in a frame called I_{EDG} . Next, if $j > 1$, preliminary segmentation was performed using a global threshold calculated by Matlab’s “graythresh” function. The mean intensity of all segmented objects was calculated. Then, the frame I_{bn} was multiplied by a factor C and added to I_{EDG} to result in I_1 , where C was calculated to ensure the bleached nucleus was three times brighter than the mean intensity of all other segmented nuclei. This procedure was to ensure that the bleached nucleus would be detected.

Next, the frame I_1 (or, if $j = 1$, frame I_{EDG}) was saturated by 5% at both ends. In other words, the 5th and 95th percentile intensities, i_5 and i_{95} , respectively, were found, and I_1 was rescaled by:

$$I_{rs} = \frac{I_1 - i_5}{i_{95} - i_5}, \quad \text{or } I_{rs} = \frac{I_{EDG} - i_5}{i_{95} - i_5} \text{ if } j = 1$$

This resulted in a frame with 5% of its pixels less than zero, and 5% greater than one. These were set to zero and one, respectively.

Next, a watershed of the complement (one minus) of I_{rs} was calculated. The watershed image was a label image, where the pixels corresponding to each nucleus plus the cytoplasm surrounding it were given a distinct numerical label. The boundaries between cytoplasmic compartments were pixels of zero intensity (see Carrell et al., 2017). This watershed matrix served to delineate the boundaries between cytoplasmic compartments for the remainder of the analysis.

We split the frame into the pixel sets that corresponded to each cytoplasmic compartment found by watershed. Each cytoplasmic compartment was hard-thresholded at its local 25% intensity. The remaining object with the largest area (within the local watershed) was declared to be the nucleus, after eroding by a disk of one micron. All pixels outside of the largest-area object (pre-erosion) were eroded by a disk of a half micron then declared to be cytoplasm. The two erosion operations were performed to get conservative estimates of what is the nucleus and what is the cytoplasm. This process was repeated for each cytoplasmic compartment in each frame of the image sequence. Afterwards, the mean intensity of each object declared to be a nucleus was calculated. Every object that was either less than 30% of this mean intensity, or less than 2.15 square microns in area, was removed.

To determine the identity of a nucleus from one frame to the next, we used a second image stabilization procedure (see STAR methods and Carrell et al., 2017), which predicted the direction of movement of the nuclei from one frame to the next. Briefly, frame j and frame $j - 1$ were Gaussian blurred with a width parameter of 10 pixels. The difference between the two blurred frames was called I_t . For frame j , gradients in the x and y directions were calculated by differencing by columns or rows, respectively, to result in arrays I_x and I_y , respectively. (Note that the differencing procedure results in an array with one fewer row or column. Because of this, I_t was intentionally reduced by one row and one column, I_x was intentionally reduced by one row, and I_y was intentionally reduced by one column.) Now let the pixels corresponding to nucleus k identified in frame j to be pixel indices in vector v_k . If the nucleus moves as a rigid body from frame $j - 1$ to frame j , and any change in intensity occurs uniformly across the whole nucleus, then the following equation holds:

$$I_x(v_k)\Delta x + I_y(v_k)\Delta y - \Delta f = -I_t(v_k)$$

...where Δx and Δy are the displacements of the nucleus, and Δf is the change in intensity from frame $j - 1$ to frame j . In practice, however, the nucleus may change shape slightly, and its intensity may change in a non-uniform fashion. Therefore, this equation becomes an over determined system with N_k equations and three unknowns (Δx , Δy , and Δf), where N_k is the number of pixels in the object declared to be nucleus k . Using linear least squares results in an estimate of Δx and Δy . With these estimates for each nucleus in frame j , the identity of each nucleus from frame 1 to the final frame can be connected. In some cases, a nucleus identified in frame $j - 1$ will not be identified as an object in frame j . In this case, this object is dropped for one or more frames; however, it may reappear in subsequent frames.

The timecourse data for the nuclear intensity were then fit to the solution of a differential equation that described the nuclear concentration of DI:

$$\frac{d[DI]_{nuc}}{dt} = k_{out}(K_{nuc}[DI]_{cyt} - [DI]_{nuc})$$

...where $[DI]_{nuc}$ and $[DI]_{cyt}$ are the nuclear and cytoplasmic concentrations of DI, respectively, k_{out} is the nuclear export rate constant for DI, and K_{nuc} is the equilibrium constant for nuclear import/export of DI, defined as $K_{nuc} = k_{in}/k_{out}$, where k_{in} is the nuclear import rate constant for DI. This is the relevant difference between our work in this paper vs the work in (Carrell et al., 2017): we parameterized our equations by K_{nuc} instead of k_{out} . We found this resulted in a more robust fit to our data.

The cytoplasmic concentration timecourse measurements served as input to this equation, and the nuclear concentration timecourse measurements were the target of the fit.

For a general function $[DI]_{cyt}(t)$, the solution to this differential equation is:

$$[DI]_{nuc}(t) = c_0 \exp(-k_{out}t) + K_{nuc}k_{out} \exp(-k_{out}t) \int_0^t [DI]_{cyt}(t') \exp(k_{out}t') dt'$$

...where $t = 0$ corresponds to the time point directly after bleaching, and c_0 is an adjustable parameter that corresponds to the concentration of nuclear DI at time $t = 0$. The fits were performed with Matlab's `lsqcurvefit` function.

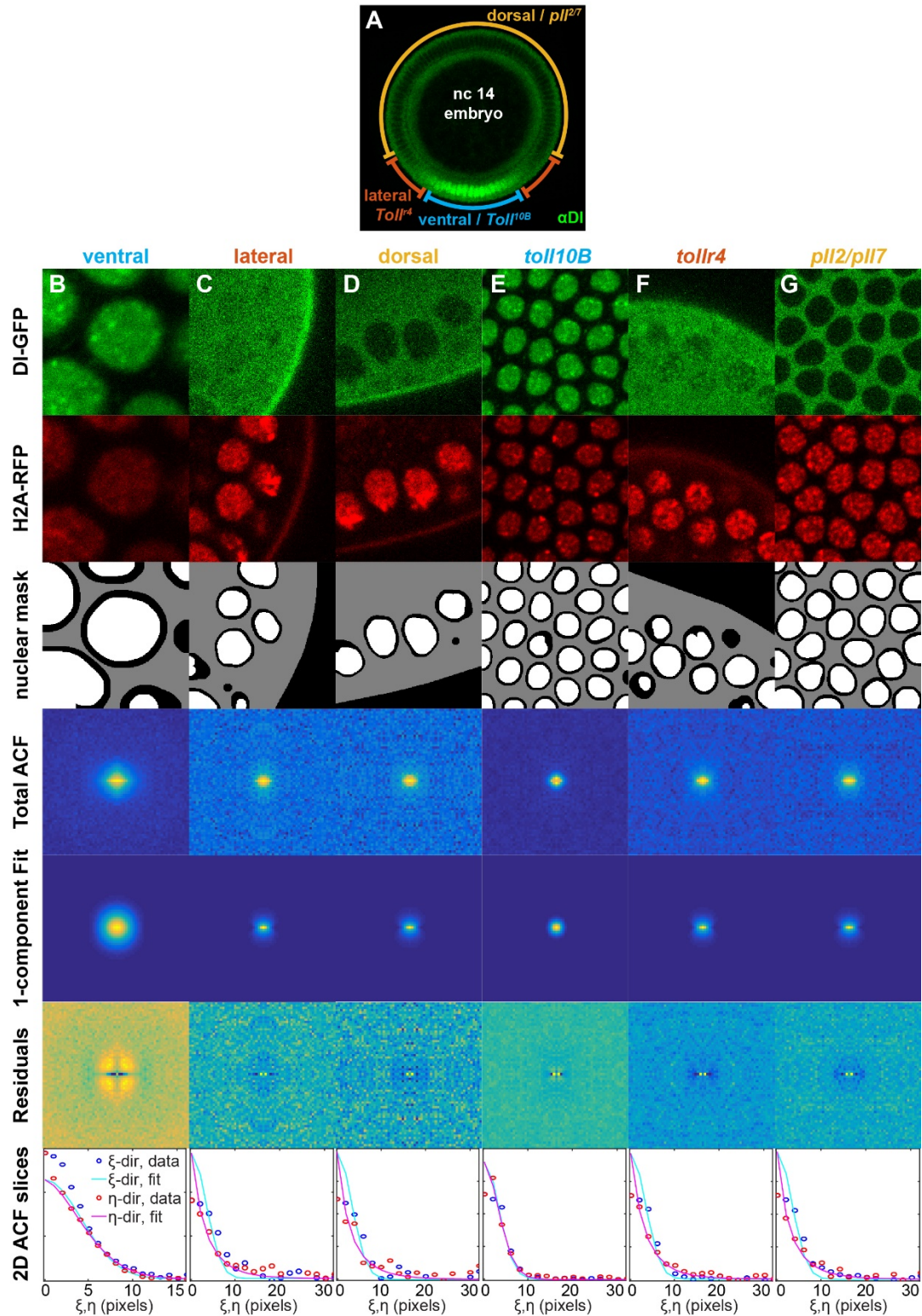


Figure S1: Representative RICS images and ACFs. (A) Fixed nc 14 embryo stained for the DI gradient (same illustration as in Fig. 5). The annotations indicate regions of the embryo that correspond to ventral, lateral, and dorsal. The mutant genotypes included denote that Toll10b is “ventral-like”, Tollr4 is “lateral-like”, and pll2/7 is “dorsal-like”. (B-D) Representative RICS analyses, including snapshot of the DI-GFP channel

and H2A-RFP channel, the nuclear and cytoplasmic masks, the heatmap of the ACF for total RICS, the ACF for the one-component model fit, the residuals to the fit, and the slices of the ACF in the fast and slow directions. Note that the nuclear mask is in white, and the cytoplasmic mask in gray. The residuals are defined as the Total ACF minus the fitted ACF. In the 2D slices plots, open circles are data, and solid curves are the best fit. Blue open circles and cyan solid curve correspond to the fast direction (ξ), while red open circles and magenta solid curve correspond to the slow direction (η). (B) Ventral side. (C) Lateral region. (D) Dorsal side. (E) Toll10b embryo. (F) Tollr4 embryo. (G) pll2/7 embryo. Related to Fig. 1.

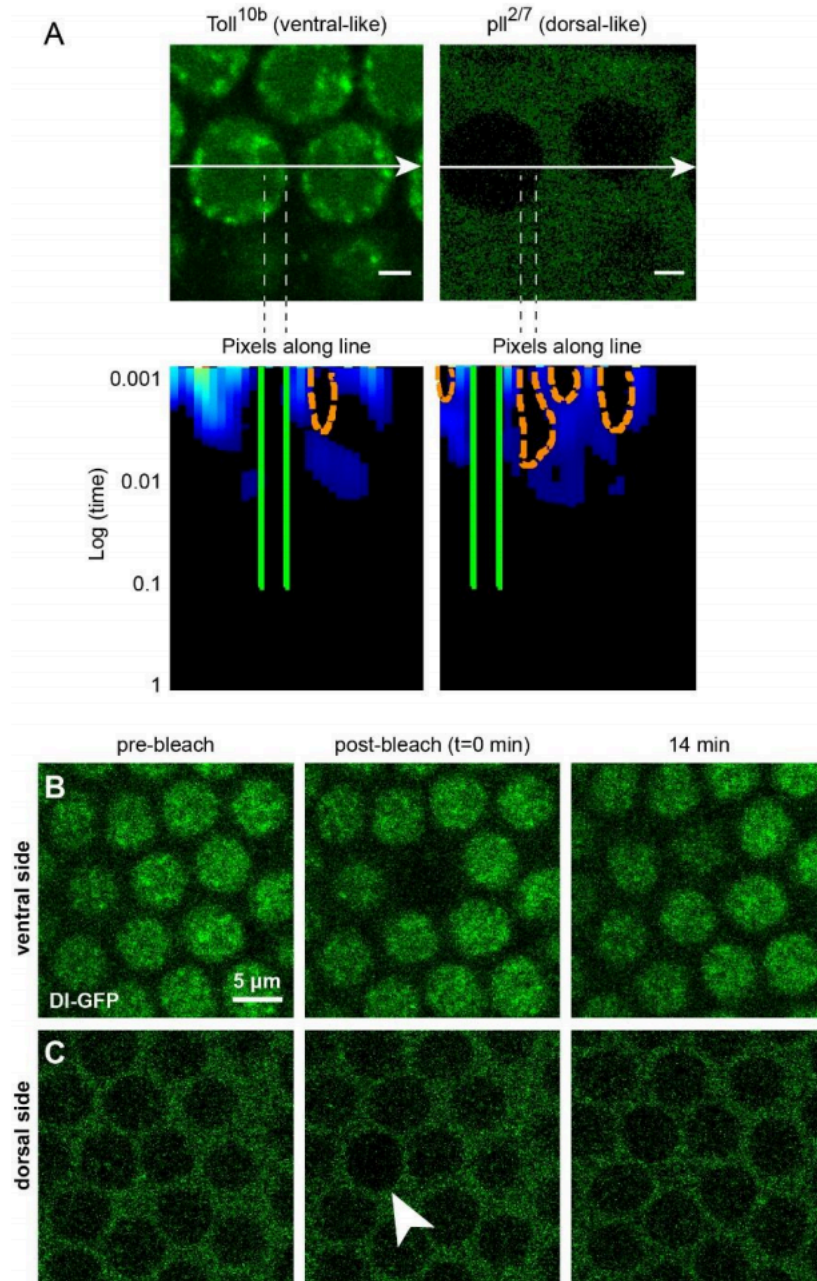


Fig. S2. **pCF and FRAP measurements of movement of DI-GFP in and out of the nucleus.** (A) Representative pCF analyses for Toll10b (left column) and pll2/7 (right column) embryos. Top row: image frame of region where pCF was performed. Bottom row: pCF carpets that correspond to the images in the top row. Scale bar = 2 μ m. Arrow represents the direction of the line scan. Orange, dashed lines in the carpet label arches which indicate delayed DI-GFP movement, while green, solid lines demarcate black regions of the carpet which indicate no DI-GFP movement. Toll10b is “ventral-like” and pll2/7 is “dorsal-like”. (B-C) Representative snapshots of FRAP experiments for times given at the top of the images for the ventral (B) and dorsal (C) sides of the embryo. Movies of full timecourses for the embryos in (B) and (C) are in Movies S4 and S5, respectively. Arrowhead in (C) indicates the bleached nucleus.

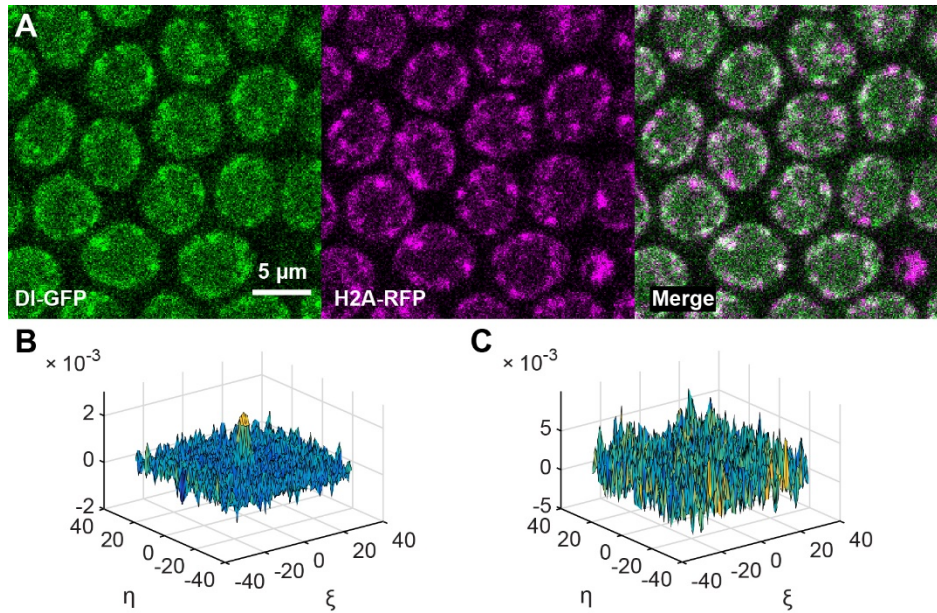


Figure S3: Cross correlation between DI-GFP and H2A-RFP. (A) Snapshot of Toll^{10b} embryo with high correlation between DI-GFP (green) and H2A-RFP (magenta). The correlation can be seen visually, as noted by the white regions in the nuclei in the merged image. (B) Cross-correlation function for the timecourse shown in (A). (C) Cross correlation function for a timecourse from a pll^{2/7} embryo, in which no correlation is found. Related to Fig. 3.

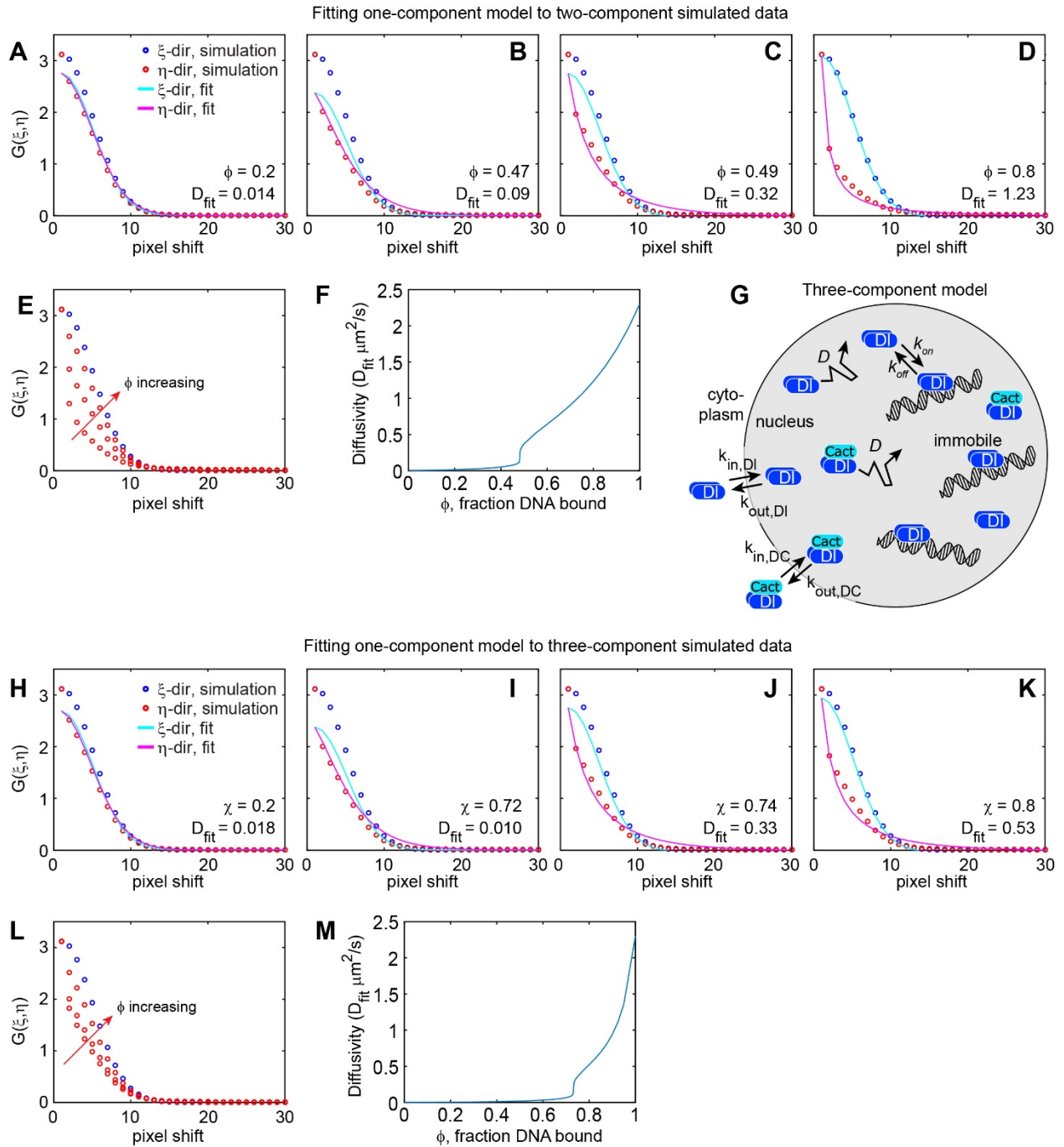
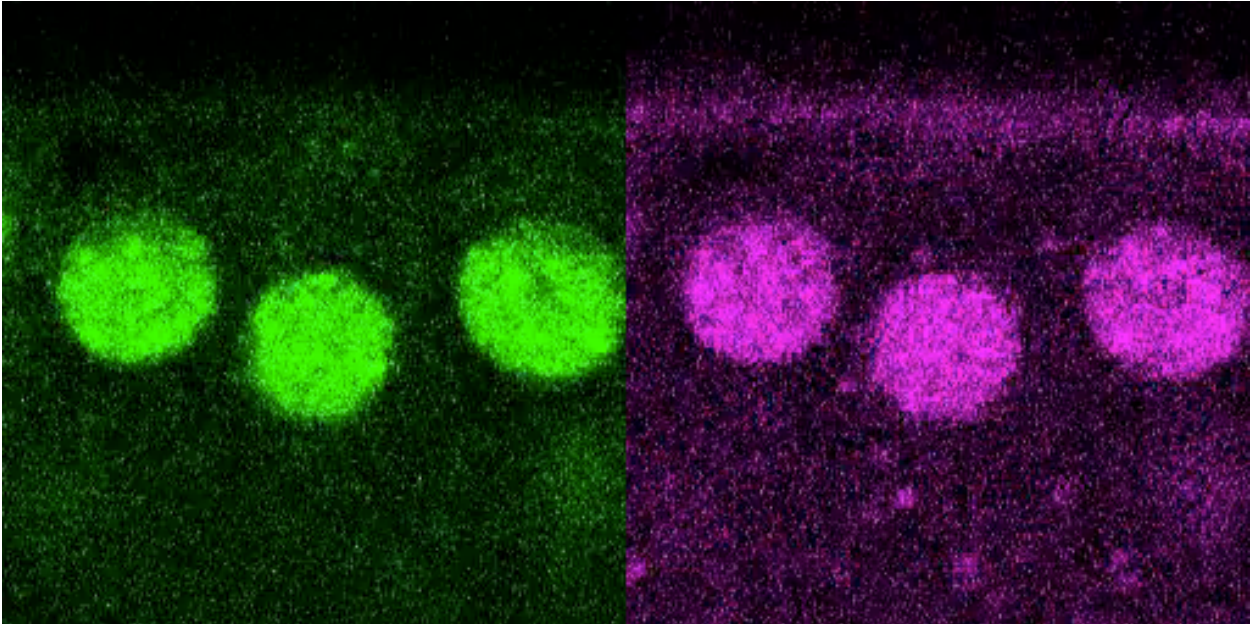
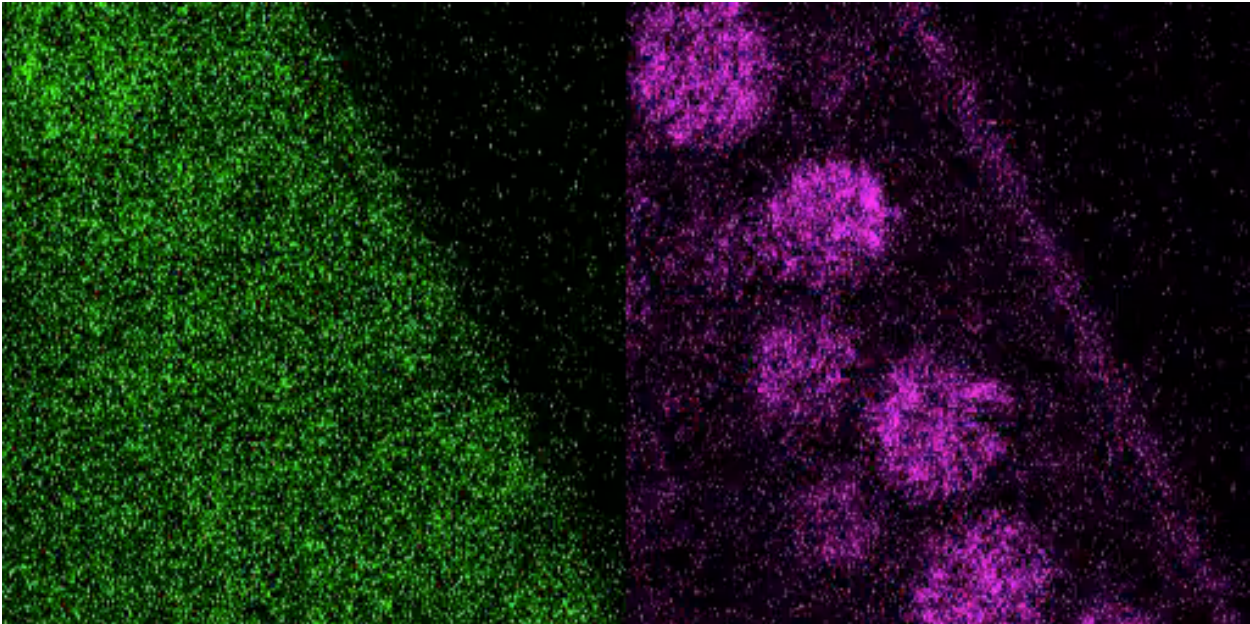


Figure S4: Fitting the one-component model to simulated ACFs from the two- and three-component models. (A). (B). Related to Fig. 4.

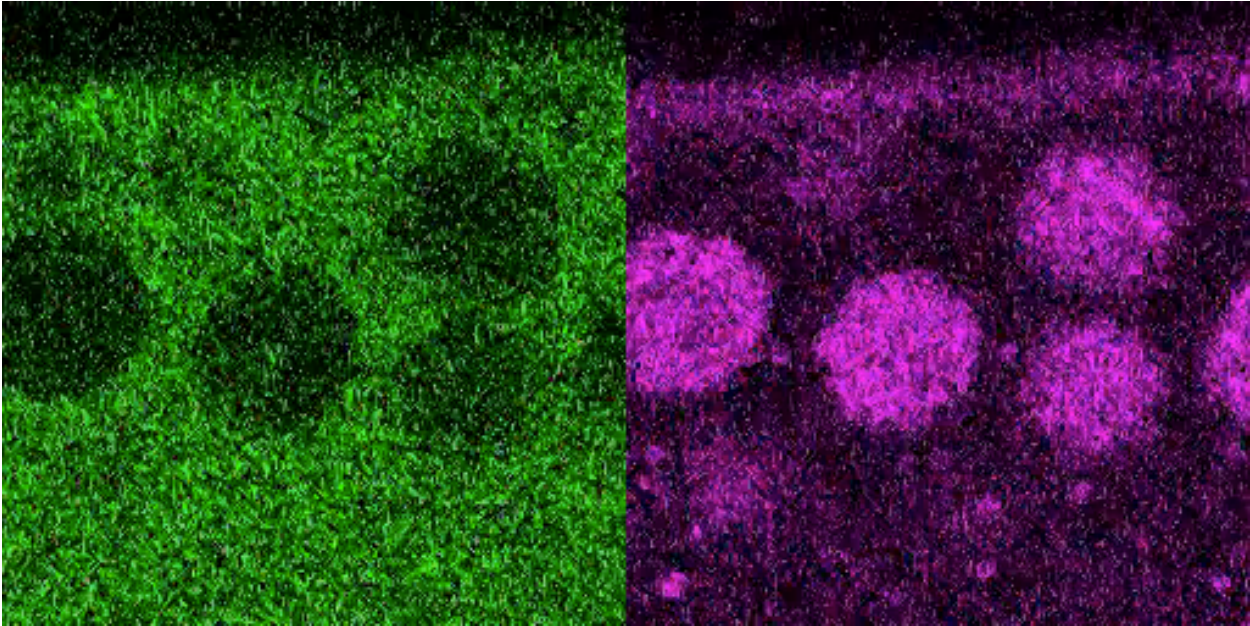
Movie S1



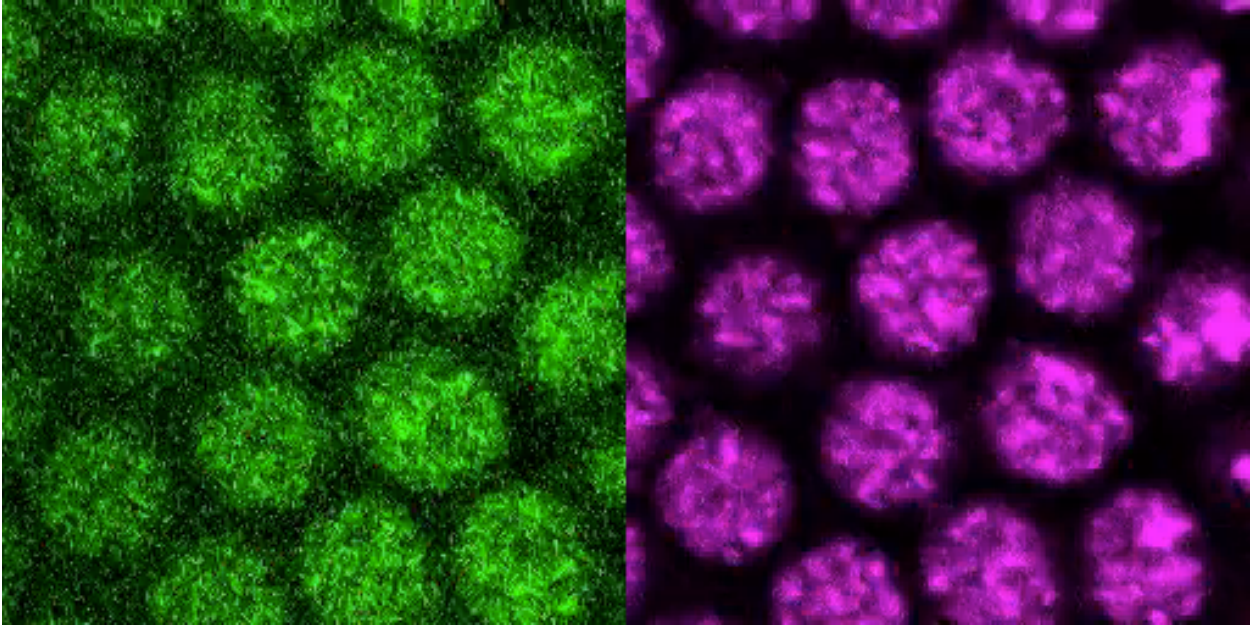
Movie S2



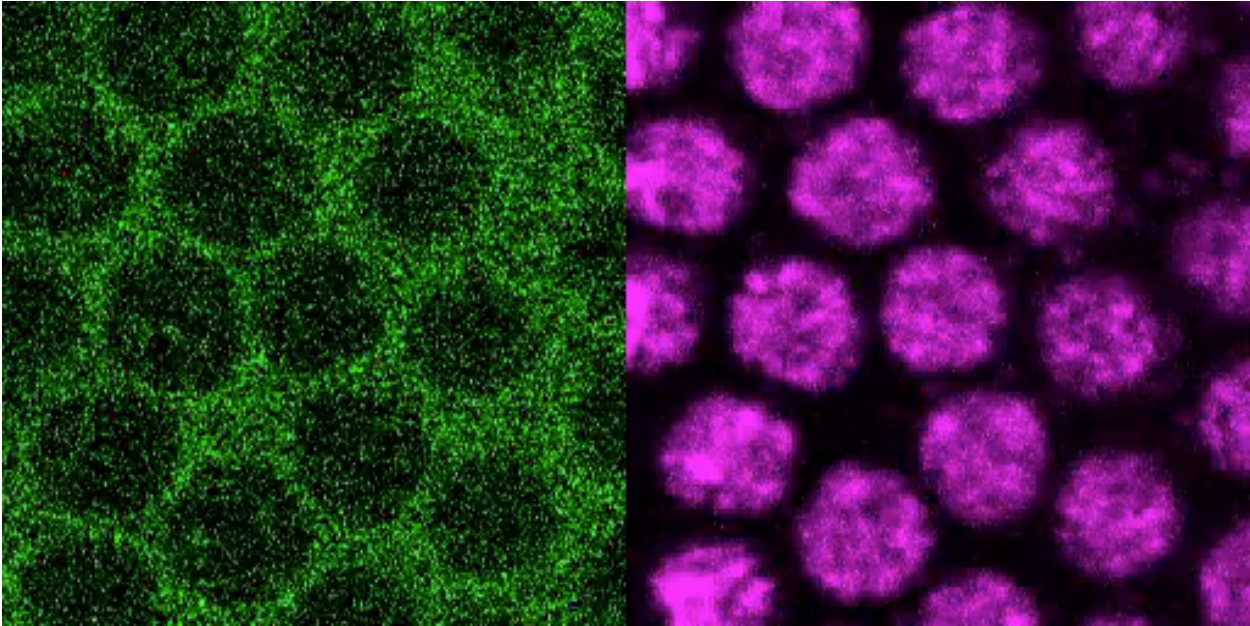
Movie S3



Movie S4



Movie S5



Movie S6

